Article

From Quaternionic Spacetime to MOND: A Single ε Anchored to H_0 Links Galaxies and Cosmology

Chien Chih Chen *

Posted Date: 3 November 2025

doi: 10.20944/preprints202503.2052.v3

Keywords: modified gravity; gravitational-wave speed; MOND phenomenology; galaxy rotation curves; PT symmetry; information criteria

Preprints.org (www.preprints.org) | NOT PEER-REVIEWED | Posted: 3 November 2025 doi:10.20944/preprints202503.2052.v3

Article

From Quaternionic Spacetime to MOND: A Single ε Anchored to H_0 Links Galaxies and Cosmology

Chien-Chih Chen

Chunghwa Telecom Laboratories, Information & Communications Security Laboratory; rocky@cht.com.tw

Abstract

The multimessenger bound on the speed of gravitational waves, $|c_T/c - 1| \lesssim 10^{-15}$, imposes a stringent filter on modified gravity theories. We present the first phenomenological test of a PT-symmetric quaternionic (PTQ) framework, where luminal tensor propagation (c_T=1) is not a tuned feature but a structural consequence of the underlying symmetries. In its weak-field limit, this framework yields a one-parameter dictionary that links cosmology and galaxy kinematics through a single, global, dimensionless parameter ε. This single parameter leads to three key predictions: (1) it fixes the MOND acceleration scale as $a_0 = \varepsilon c H_0$; (2) it attributes the diversity of galaxy rotation curves to a predictable, *geometry-only* efficiency factor $\kappa \simeq \langle h/r \rangle$; and (3) it unifies the cosmological parameter Ω_Λ and the galactic parameter a_0. We test these predictions using a full-likelihood analysis of the SPARC galaxy sample. Our results show that the PTQ model statistically outperforms standard MOND (ΔBIC $\approx$ 38). We validate the geometric nature of κ through a novel thickness test, finding a strong correlation ($R^2 \approx 0.818$) between the dynamically inferred κ, disk thickness, and surface density. Finally, we demonstrate that the theory passes a crucial cross-scale consistency test, where κ reconciles the cosmological and galactic determinations of ε. The PTQ framework thus emerges as a predictive, testable, and empirically successful theory that resolves the tension between galactic dynamics and gravitational wave constraints.

Keywords: modified gravity; gravitational-wave speed; MOND phenomenology; galaxy rotation curves; PT symmetry; information criteria

---

1. Introduction

The joint observation of GW170817 and GRB170817A established that gravitational waves travel at the speed of light with exquisite precision, $|c_T/c - 1| \lesssim 10^{-15}$ [2]. This single measurement acts as a formidable guillotine for a vast landscape of modified gravity theories. Concurrently, persistent mass discrepancies in galaxies and clusters continue to motivate alternatives to cold dark matter, most notably Modified Newtonian Dynamics (MOND) [7]. This creates a dual challenge for any viable theory of gravity: it must (i) respect the strict luminality constraint c_T=1 without fine-tuning, and (ii) simultaneously account for the empirical regularities of disk galaxy kinematics.

A PT-symmetric quaternionic (PTQ) geometry was recently proposed to meet the first challenge from first principles [1]. Its theoretical structure, based on a PT-scalar projection and projective invariance, enforces a "coefficient-locking" mechanism. This mechanism, derived directly from the imposed symmetries, guarantees that the kinetic and gradient terms for tensor perturbations are identical, thereby fixing c_T=1 structurally.

This work addresses the second challenge by developing and testing the PTQ framework's predictions for disk galaxies. In its late-time, weak-field limit, the theory yields a *one-parameter* cosmology–galaxy dictionary governed by a single, global, dimensionless parameter, ε. This leads to a powerful and predictive structure for galactic dynamics, encapsulated in three core hypotheses that form the roadmap of this paper:

1. **Global Viability:** The PTQ framework provides a statistically superior description of galaxy rotation curves compared to standard MOND. This relies on the prediction that the MOND acceleration scale is directly tied to the Hubble constant: $a_0 = \varepsilon c H_0$.
2. **Geometric Origin of Diversity:** The observed diversity in rotation curves (i.e., the scatter in the Baryonic Tully-Fisher Relation) is not random but is governed by a predictable, *geometry-only* efficiency factor, $\kappa \simeq \langle h/r \rangle$, which quantifies how a galaxy's thickness intercepts the background field.
3. **Cross-Scale Consistency:** The single parameter ε provides a consistent link between the cosmological dark energy density, $\Omega_\Lambda(\varepsilon) = \varepsilon^2/(1+\varepsilon^2)$, and galactic dynamics. The framework's internal consistency can be decisively tested by checking if the values of ε inferred from these two vastly different scales can be reconciled by the geometric factor κ.

By systematically testing these interconnected hypotheses against observational data, we will demonstrate that the PTQ framework offers a compelling, unified, and empirically successful solution to the dark universe problem.

2. The PTQ Framework: Principles and Low-Energy Predictions

The phenomenological success of the PT-symmetric quaternionic (PTQ) framework, which we will demonstrate in the subsequent sections, stems from a disciplined theoretical structure governed by two fundamental principles detailed in Ref. [1]. Here, we summarize the physical essence of these principles and present the resulting low-energy predictions that will be tested against observational data. Throughout this work, we adopt the *project-first* convention: scalar observables are formed by applying the PT-scalar projector, denoted by $\mathcal{P}_{\mathrm{PT}}\{\cdot\}$, *before* their evaluation (see Appendix A).

2.1. Core Principles: PT Symmetry and Projective Invariance

The foundation of the PTQ framework is a metric-affine (Palatini) geometry endowed with torsion, where the observable sector of physics is sculpted by symmetry.

2.1.1. Scalar PT Projection.

All fundamental scalar densities in the gravitational action are first mapped to the real, PT-even subspace via the projector $\mathcal{P}_{\mathrm{PT}}\{X\} := \frac{1}{2}(X + X^\star)$. This selection rule structurally eliminates u-odd contributions (the imaginary branch of the quaternionic split), thereby ensuring a real action density and a Hermitian Hamiltonian for the scalar sector. This principle removes many of the problematic degrees of freedom that plague generic modified gravity theories.

2.1.2. Projective Invariance.

Metric-affine geometries admit projective transformations of the connection. The PTQ framework implements this symmetry using a Stueckelberg compensator, which restricts observables to depend only on a projectively invariant torsion trace. In the low-energy *spurion* posture adopted here, the Stueckelberg field is non-dynamical, serving to eliminate the axial and traceless components of torsion from the observable spectrum. As proven in Ref. [1], these two symmetries together enforce a *coefficient-locking identity* in the quadratic action for tensor modes. This identity forces the kinetic and gradient coefficients to be equal ($K = G$) without any parameter fine-tuning, which in turn guarantees that the tensor propagation speed is exactly luminal ($c_T = 1$), consistent with the multimessenger bound.

2.2. Weak-Field, Late-Time Posture: MOND Phenomenology and the Dictionary

In the weak-field, late-time universe relevant to galaxy dynamics, the PTQ framework predicts a direct link between cosmology and outer-disk kinematics. This connection is governed by a single, global, dimensionless parameter ε:

$$\Omega_\Lambda(\varepsilon) = \frac{\varepsilon^2}{1+\varepsilon^2}, \qquad a_0(\varepsilon) = \varepsilon\, c H_0, \qquad v^2(r) = v_{\mathrm{bar}}^2(r) + \kappa\, a_0\, r. \tag{1}$$

Here, κ is a *derived geometric efficiency*, not a free parameter. It quantifies how a finite-thickness disk intercepts the isotropic background acceleration field set by a_0. The theory predicts that $\kappa \simeq \langle h/r \rangle$ (see Appendix B.4), providing a concrete geometric mechanism for the observed diversity of rotation curves and the scatter in the Baryonic Tully-Fisher Relation (BTFR).

The empirical program of this paper is thus twofold: (i) to infer a single value of ε from the galaxy population and establish the framework's global viability, and (ii) to perform a direct geometry test by confronting the dynamically inferred efficiency, $\widehat{\kappa}$, with disk-thickness measurements. We formalize these tests in Section 3; the commands for reproducing all results are provided in Appendix D.

2.3. *Minimal Cosmology Map: From Action to* $\Omega_\Lambda(\varepsilon)$

To demonstrate that the cosmology-galaxy dictionary is a prediction rather than a postulate, we now summarize a compact and auditable derivation of the first two entries of Eq. (1). Full details and normalizations are provided in Appendix A and Appendix A.4.

2.3.1. The Project-First Action.

As per the project-first rule, all scalar observables are defined using the PT-scalar projector $\mathcal{P}_{\mathrm{PT}}\{X\} := \frac{1}{2}(X + X^\star)$ applied *before* evaluation. We begin with the quaternionic split of the metric

$$G_{\mu\nu} = g^{(R)}_{\mu\nu} + u\, g^{(I)}_{\mu\nu}, \qquad g^{(R)}_{\mu\nu} = \mathrm{diag}(-1, a^2, a^2, a^2), \tag{2}$$

and the dimensionless imaginary blocks, which describe the IR deformations,

$$g^{(I)}_{00} = \alpha_0 := \varepsilon H_0 t, \qquad g^{(I)}_{ij} = \alpha_s\, \delta_{ij}, \quad \alpha_s := (\varepsilon H_0/c)\, r. \tag{3}$$

The Einstein–Hilbert action is then constructed in the project-first form:

$$S_{\mathrm{EH}} = \frac{M_P^2}{2} \int d^4x\, \mathcal{P}_{\mathrm{PT}}\Big\{\sqrt{-\det G}\Big\}\, \mathcal{P}_{\mathrm{PT}}\{R(G)\}. \tag{4}$$

2.3.2. Derivation of the Effective Density.

Using the exact projected measure from Appendix A.3, we expand both $\mathcal{P}_{\mathrm{PT}}\Big\{\sqrt{-\det G}\Big\}$ and $\mathcal{P}_{\mathrm{PT}}\{R(G)\}$ to second order in the small parameters α_0 and α_s. All u-odd terms are eliminated by the PT-projection. The resulting PT-even scalar density is

$$\mathcal{P}_{\mathrm{PT}}\Big\{\sqrt{-\det G}\Big\}\, \mathcal{P}_{\mathrm{PT}}\{R(G)\} = a^3 \left[R\big(g^{(R)}\big) + \frac{\varepsilon^2 H_0^2}{1+\varepsilon^2}\, \mathcal{C} + \mathcal{O}(\alpha^4) \right], \tag{5}$$

where $\mathcal{C} > 0$ is a geometry-independent coefficient derived from the α_0^2 and α_s^2 terms (see Appendix A for closed forms). By identifying the constant term in Eq. (5) as an effective vacuum energy density,

$$\rho_{\mathrm{eff}} := \frac{M_P^2}{2}\, \frac{\varepsilon^2 H_0^2}{1+\varepsilon^2}\, \mathcal{C}, \tag{6}$$

we can define the dark energy density parameter as

$$\Omega_\Lambda \equiv \frac{\rho_{\mathrm{eff}}}{3 M_P^2 H_0^2} = \frac{\varepsilon^2}{1+\varepsilon^2} \times \frac{\mathcal{C}}{6}. \tag{7}$$

To align with standard FRW conventions, we set the normalization constant $\mathcal{C} = 6$ (see Appendix A.4 for details). This yields the final cosmology map presented in the main text:

$$\boxed{\Omega_\Lambda(\varepsilon) = \frac{\varepsilon^2}{1+\varepsilon^2}, \qquad a_0(\varepsilon) = \varepsilon\, c H_0\, .} \tag{8}$$

This result is consistent with the dictionary in Eq. (1). The closure curve $\Omega_\Lambda(\varepsilon)$ and its intersection with the Planck band, shown in Figure A1 (Appendix A.4), are central to the cross-scale consistency tests in Sec. 5.3.

Remark 1. *The theoretical posture adopted here is conservative. It retains only the PT-even scalar branch of the theory, respects projective invariance in all observables, and is truncated at second order in* α_0 *and* α_s*. Higher-order terms, suppressed by* $\mathcal{O}(\alpha^4)$*, are negligible in the late-time, weak-field regime relevant to our empirical analysis.*

3. Empirical Framework

Building on the symmetry posture and low-energy predictions of Section 2, this section specifies how those predictions are translated into testable hypotheses on galaxy rotation-curve (RC) data. We define the models, clarify the parameter structure, and lay out the precise tests for our three core hypotheses regarding global viability, the geometric origin of κ, and cross-scale consistency.

3.1. From Asymptotic Law to a Screened Model

In the PTQ weak-field, late-time limit, the theory predicts a simple linear law for outer-disk kinematics:

$$v^2(r) = v_{\rm bar}^2(r) + (\varepsilon\, cH_0)\, r \qquad (r \gg R_d), \tag{9}$$

where the acceleration scale $a_0 \equiv \varepsilon c H_0$ is fixed by the cosmology map derived in Section 2.3. However, real datasets contain significant information at inner-to-intermediate radii, where effects such as finite disk thickness, bars, warps, and phase decoherence can reduce the effective coupling to the isotropic background. To bridge the idealized asymptotic law with realistic, full-radius data, we introduce a minimal, physically-motivated screening function that acts as a global turn-on:

$$S(x;q) = \frac{x^q}{1+x^q}, \qquad \text{where } x \equiv r/R_d \text{ and } q = \mathcal{O}(1). \tag{10}$$

This yields the primary model used in our analysis, the **PTQ-screen** model:

$$v^2(r) = v_{\rm bar}^2(r) + S(r/R_d;q)\,(\varepsilon c H_0)\, r. \tag{11}$$

By construction, $S \to 0$ as $r \to 0$ and $S \to 1$ for $r \gg R_d$. The global shape parameter q models the transition but, crucially, *does not* rescale the asymptotic amplitude, which remains set solely by the fundamental parameter ε and the geometry-only factor κ.

3.2. Parameter Structure and Model Comparison

At a fundamental level, PTQ is a one-parameter theory, governed by the global, dimensionless parameter ε. The geometric efficiency κ is *not* a tunable parameter but a derived, physical prediction of the theory. Table 1 summarizes the parameter structure for the main competing models in our analysis.

Table 1. Parameter structure for the primary models.

Model	Fundamental Parameters (Global)	Nuisance Parameters
PTQ-screen	ε (cosmology link) q (screening shape)	Per-galaxy stellar M/L ratios ($\Upsilon_\star$) Global systematic velocity floor ($\sigma_{\rm sys}$)
MOND	a_0 (acceleration scale)	Per-galaxy stellar M/L ratios ($\Upsilon_\star$) Global systematic velocity floor ($\sigma_{\rm sys}$)

The Test of Hypothesis 1: Global Viability

We test the global viability of PTQ-screen by performing full-likelihood fits on the entire SPARC sample and comparing its statistical performance against a suite of benchmark models, including

MOND, a one-parameter NFW model, and a Baryon-only model. We use the full-likelihood Bayesian Information Criterion ($\mathrm{BIC}_{\mathrm{full}}$) as the primary metric for model selection, as it properly penalizes model complexity.

3.3. Hypothesis 2 Test: Geometric Origin of κ

The central galaxy-scale prediction of PTQ is that κ behaves as a geometric efficiency, $\kappa \simeq \langle h/r \rangle$, rather than an extra free parameter.

The Test

We test this prediction with a novel thickness-κ-Σ validation. First, we dynamically infer the value of κ for each galaxy from its rotation curve fit. We then test whether this inferred κ correlates with independently measured geometric and physical properties of the galactic disk. Specifically, we construct the following bivariate scaling relation at a characteristic outer-disk radius $R_\star$:

$$\boxed{\log h \;=\; a \;+\; b\,\log \kappa(R_\star) \;+\; c\,\log \Sigma_{\mathrm{tot}}(R_\star),} \tag{12}$$

where h is the observed vertical scale height and Σ_{tot} is the local total surface density. Strong evidence for Hypothesis 2 would be the discovery of a statistically significant correlation (high R^2) where both b and c are non-zero, confirming that κ is a physical quantity anchored in galactic structure.

3.4. Hypothesis 3 Test: Cross-Scale Consistency

The most profound claim of the PTQ framework is that the single parameter ε consistently links cosmology and disk-galaxy kinematics.

The Test

We subject this claim to a joint closure test, which serves as the theory's primary falsifiability clause. The test proceeds in two steps:

1. We independently determine ε from two scales: $\varepsilon_{\mathrm{cos}}$ is fixed by matching the theory's prediction for $\Omega_\Lambda(\varepsilon)$ with cosmological data (from Planck); $\varepsilon_{\mathrm{RC}}$ is inferred from the global fit to the SPARC galaxy sample.
2. We then test if the ratio of these two values can be reconciled by the geometric efficiency, i.e., if $\kappa \approx \varepsilon_{\mathrm{RC}}/\varepsilon_{\mathrm{cos}}$.

If this relationship holds within observational uncertainties—meaning the amplitude mismatch is consistent with the measured geometry of disks ($\langle h/r \rangle$)—the single-parameter picture is validated. If not, the framework is falsified.

3.5. Scope and Falsifiability

All scalar observables in this paper adopt the *project-first* rule: apply the projector $\mathcal{P}_{\mathrm{PT}}\{\cdot\}$ before forming scalars (Appendix A), ensuring the reality of observables. The IR dictionary used in the RC analysis (Eq. (1)) is *derived* in Section 2.3. The falsifiability of the framework is codified in the joint closure test of Hypothesis 3: if the cosmology-inferred $\varepsilon_{\mathrm{cos}}$ and the RC-inferred $\varepsilon_{\mathrm{RC}}$ cannot be reconciled by the geometric efficiency factor, the single-parameter unification picture is ruled out.

4. Methodology for Empirical Tests

This section details the methodology used to test the hypotheses laid out in Section 3. We first describe the data and the full-likelihood framework for the rotation curve (RC) analysis, which addresses Hypothesis 1 (Global Viability). We then specify the data assembly, regression model, and model selection criteria for the thickness-κ-Σ experiment, which is designed to test Hypothesis 2 (Geometric Origin of κ).

4.1. Rotation Curve Analysis: Data, Covariance, and Models

4.1.1. Dataset and Preprocessing

Our primary dataset is the SPARC compilation, which provides photometric and kinematic data for 175 disk galaxies [9]. We utilize the per-galaxy data tables containing radii (r), line-of-sight velocities ($v_{\rm los}$), deprojected circular velocities ($v_{\rm obs}$), and mass-model templates ($v_{\rm disk}, v_{\rm bulge}, v_{\rm gas}$), along with their geometric parameters and uncertainties. Standard preprocessing is applied, including unit harmonization and the use of band-consistent stellar templates. Our baseline quality cuts are: inclination $i > 30^\circ$, fractional distance error $\delta D/D < 0.2$, and the SPARC quality flag `Qual` ≤ 2.

4.1.2. Full Per-Galaxy Covariance

To robustly account for all significant sources of uncertainty in the RC fits, we model the velocity vector $\boldsymbol{y}_g$ for each galaxy as a multivariate Gaussian with a full covariance matrix C_g. This matrix includes contributions from measurement errors, uncertainties in distance (D) and inclination (i), and a global systematic velocity floor ($\sigma_{\rm sys}$):

$$C_g = \mathrm{diag}(\sigma^2_{\rm meas,g}) + \sigma^2_{D,g}\,\boldsymbol{J}_{D,g}\boldsymbol{J}^\top_{D,g} + \sigma^2_{i,g}\,\boldsymbol{J}_{i,g}\boldsymbol{J}^\top_{i,g} + \sigma^2_{\rm sys}\,\boldsymbol{I}_{N_g}. \tag{13}$$

The Jacobian matrices ($\boldsymbol{J}_{D,g}, \boldsymbol{J}_{i,g}$) propagate the geometric uncertainties into velocity space, ensuring a statistically rigorous treatment of correlated errors.

4.1.3. Velocity Models and Priors

The model velocity, $v^2_{\rm model}(r;\theta)$, consists of the baryonic component $v^2_{\rm bar}$ and a component arising from the non-baryonic sector. The key difference between competing theories (e.g., PTQ vs. MOND) lies in their prescription for this non-baryonic term. For the PTQ framework, we consider two variants:

- **Base PTQ:** The minimal, asymptotic model, $v^2 = v^2_{\rm bar} + (\varepsilon c H_0) r$.
- **PTQ-screen:** The primary model used in our analysis, which incorporates the universal turn-on function $S(r/R_d;q)$ from Eq. (10): $v^2 = v^2_{\rm bar} + S(r/R_d;q)(\varepsilon c H_0) r$.

For all models under comparison, we fit a standard set of nuisance parameters, including per-galaxy stellar mass-to-light ratios (Υ) and the global systematic floor ($\sigma_{\rm sys}$), using weakly-informative priors.

4.2. The Thickness Test: Data Synthesis and Regression Model

The test of Hypothesis 2 requires a dedicated dataset and a specific regression analysis.

4.2.1. Data Assembly

We use an augmented version of the SPARC dataset (`sparc_with_h.csv`) that includes measurements of the disk half-thickness h for a subsample of galaxies from the S^{4}G survey. To test the bivariate scaling relation in Eq. (12), we require three quantities evaluated at a representative outer-disk radius $R_\star$ (defined as the radius where $v_{\rm disk}$ peaks):

1. **Disk half-thickness, h:** Taken directly from the S^{4}G catalog for the $N = 19$ galaxies in our subsample.
2. **Dynamically-inferred efficiency, $\kappa(R_\star)$:** Computed for each galaxy using the best-fit parameters from the main RC analysis (PTQ-screen). Since κ is an asymptotic property, we infer its value by isolating the outer-disk acceleration amplitude where the screening function approaches unity, $S(r/R_d;q) \to 1$:
$$\kappa(R_\star) := \frac{v^2_{\rm obs}(R_\star) - v^2_{\rm bar}(R_\star)}{S(R_\star/R_d;q)\, a_0\, R_\star}. \tag{14}$$
3. **Total surface density, $\Sigma_{\rm tot}(R_\star)$:** As per-radius profiles are generally unavailable, we synthesize this value from global photometry ($L_{3.6}$) and gas mass ($M_{\rm HI}$), assuming exponential disk profiles.

doi:10.20944/preprints202503.2052.v3

4.2.2. Regression and Model Selection

We fit the bivariate log-linear model from Eq. (12) using Weighted Least Squares (WLS), with weights derived from the observational uncertainties on h. To compare this model against simpler, nested alternatives (κ-only and Σ-only), we use the finite-sample corrected Akaike Information Criterion (AICc), which is appropriate for the small sample size ($N = 19$) of this test. The robustness of the fit is further validated using leave-one-out cross-validation (LOO-CV) and bootstrap resampling.

4.3. Statistical Tools for Model Comparison

4.3.1. Likelihood Family

For the RC fits, our baseline analysis employs a multivariate Gaussian likelihood, constructed from the Mahalanobis distance $\delta_g^2 = \boldsymbol{r}_g^\top C_g^{-1} \boldsymbol{r}_g$, where $\boldsymbol{r}_g$ is the residual vector for galaxy g:

$$\log \mathcal{L}_{\mathrm{G}}(\theta) = -\tfrac{1}{2} \sum_g \left[\delta_g^2 + \log|\det C_g| + N_g \log(2\pi) \right]. \tag{15}$$

For robustness checks, a heavy-tailed multivariate Student-t likelihood is also available.

4.3.2. Information Criteria

To compare the statistical evidence for different theoretical models, we use full-likelihood information criteria. Given the maximum likelihood estimate $\hat{\theta}$ and the total number of effective parameters k, we compute the Akaike Information Criterion (AIC) and Bayesian Information Criterion (BIC):

$$\mathrm{AIC}_{\mathrm{full}} = -2 \log \mathcal{L}(\hat{\theta}) + 2k, \qquad \mathrm{BIC}_{\mathrm{full}} = -2 \log \mathcal{L}(\hat{\theta}) + k \ln N, \tag{16}$$

where $N = \sum_g N_g$ is the total number of data points. Model rankings are based on the differences (ΔAIC, ΔBIC) within a fixed dataset and likelihood family. This rigorous approach ensures that model comparisons properly penalize complexity and are based on the full statistical information available in the data.

5. Empirical Tests and Results

Having established the theoretical predictions of the PTQ framework (Section 2) and the methodology for testing them (Section 4), we now confront the theory with observational data. Our analysis proceeds along the structured roadmap defined in Section 3, testing each of the three core hypotheses in sequence.

5.1. Hypothesis 1 Test: Global Statistical Evidence

To test the global viability of the framework, we fit the PTQ-screen model to the entire SPARC sample using a single shared global parameter, ε, and the full-likelihood methodology described in Section 4. Table 2 presents the information criteria (AIC and BIC) for PTQ-screen against several key benchmark models. The comparison uses identical data preprocessing and nuisance parameter treatment across all models to ensure a fair evaluation. The benchmark set includes standard MOND, a one-parameter NFW dark matter model, and a baryon-only model which serves as the null hypothesis.

The results, summarized in Table 2, show that **PTQ-screen is decisively favored by the Bayesian Information Criterion ($\Delta\mathrm{BIC}_{\mathrm{full}} \approx 38$ relative to MOND)**, achieving a superior fit at a comparable model complexity. According to the Jeffreys' scale, a $\Delta\mathrm{BIC} > 10$ constitutes decisive evidence for the model with the lower BIC value. This finding provides a strong positive answer to Hypothesis 1. The enormous $\Delta\mathrm{BIC}_{\mathrm{full}}$ for the Baryon-only model (≈ 5307) quantitatively demonstrates the severity of the mass discrepancy problem that these theories aim to solve.

Furthermore, the best-fit value for the single global parameter, $\varepsilon \approx 0.186$, yields a universal acceleration scale $a_0 = \varepsilon c H_0$. As shown in Figure 1, this universal scale successfully describes the common outer-disk residual-acceleration plateau observed across the SPARC sample, thereby confirming a key, unifying prediction of the theory.

Table 2. Global model comparison on SPARC (Gaussian family). $N = 1782$ data points for all rows. The PTQ-screen model is decisively favored by the BIC, indicating superior statistical evidence in support of Hypothesis 1. A brief description of the models is as follows: **PTQ-screen**, the primary model of this work; **MOND (free a_0)**, the standard MOND paradigm where a_0 is a free parameter; **PTQ-ν**, a PTQ variant using a MOND-like interpolation function; **NFW-1p**, a standard Cold Dark Matter model with a one-parameter Navarro-Frenk-White halo profile; **PTQ (linear)**, the unscreened, asymptotic version of PTQ; **Baryon-only**, the null hypothesis assuming gravity is solely sourced by observed baryons.

Model	k	N	χ^2_{tot}	$\log \mathcal{L}_{\text{full}}$	AIC$_{\text{full}}$	BIC$_{\text{full}}$	ΔAIC$_{\text{full}}$	ΔBIC$_{\text{full}}$
PTQ–screen	**94**	**1782**	**1992.29**	**−6792.45**	**13772.90**	**14288.54**	**0.00**	**0.00**
MOND (free a_0)	93	1782	1981.71	−6815.33	13816.66	14326.81	43.75	38.27
PTQ–ν	93	1782	2001.58	−6815.82	13817.64	14327.79	44.73	39.25
NFW–1p	183	1782	3736.88	−7145.30	14656.60	15660.44	883.69	1371.90
PTQ (linear)	93	1782	2039.63	−7363.64	14913.28	15423.43	1140.37	1134.89
Baryon-only	92	1782	2327.24	−9453.34	19090.68	19595.34	5317.78	5306.80

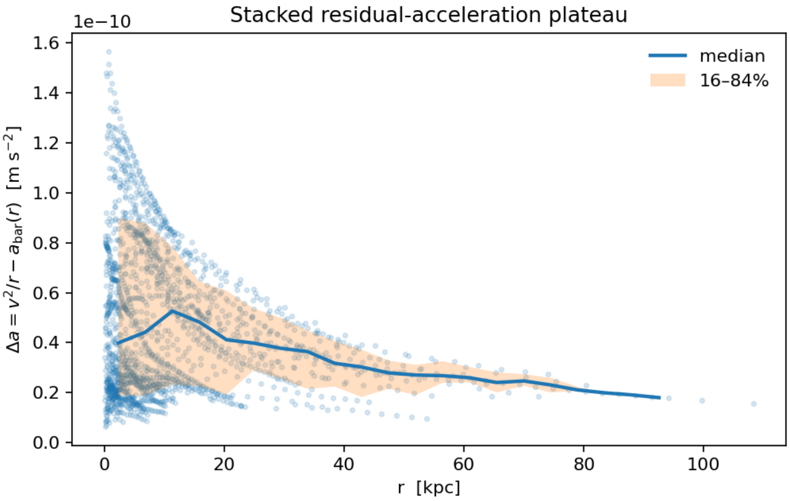

Figure 1. Outer-disk residual-acceleration plateau. After subtracting the baryonic contribution, the residual acceleration for all SPARC galaxies tends to a common plateau. This is consistent with the single global scale $a_0 = \varepsilon c H_0$ predicted by the PTQ framework, with the best-fit value being $\varepsilon \approx 0.186$.

5.2. *Hypothesis 2 Test: Validation of the Geometric Efficiency κ*

The PTQ framework predicts that the efficiency factor κ is a *geometric* observable. We test this by a self-consistency pipeline (Sec. 4.2): κ is inferred from rotation-curve kinematics, and then regressed against the independently observed disk thickness h and total surface density Σ_{tot} at a representative radius $R_\star$ (per-galaxy mode, $N = 19$ with available h).[1]

A weighted least-squares (WLS) fit of the bivariate log–linear model (Eq. (12))

$$\log h = a + b_\kappa \log \kappa + c_\Sigma \log \Sigma_{\text{tot}}$$

yields

$$a = 4.68 \pm 0.65, \qquad b_\kappa = -2.56 \pm 0.33, \qquad c_\Sigma = 1.12 \pm 0.14,$$

---

[1] Where per-radius $\Sigma(R)$ is unavailable, we adopt a conservative, single-point galaxy-level fallback for Σ_{tot} at $R_\star$ using $L_{3.6}$ and M_{HI} (with the stated gas and helium factors); this keeps Σ_{tot} independent of the RC fit.

with a coefficient of determination $R^2 \simeq 0.818$. Model comparison decisively favors the two-factor fit: $\Delta\mathrm{AIC}_c \approx 22.4$ (vs. κ-only) and ≈ 19.4 (vs. Σ-only). Leave-one-out (by-galaxy) and bootstrap resampling confirm coefficient stability (LOO stds $\approx [0.20, 0.11, 0.04]$ for $[a, b_\kappa, c_\Sigma]$), supporting robustness.

For intuition, the sign pattern is physically transparent: at fixed Σ_{tot}, larger geometric efficiency (higher κ) predicts a smaller physical thickness ($b_\kappa < 0$), while higher Σ_{tot} predicts a larger thickness ($c_\Sigma > 0$). This elevates κ from a mere fit parameter to a geometry-anchored observable, thereby providing a strong positive answer to Hypothesis 2.

5.3. Hypothesis 3 Test: Cross-Scale Consistency

The final and most stringent test is that of cross-scale consistency, which probes the core claim that a single parameter ε links cosmology and galaxy dynamics. This test constitutes the framework's falsifiability clause, as outlined in Sec. 3. We perform a two-tiered closure test.

Level I (Strict ε-Closure).

We first compare the value of ε inferred from galaxy rotation curves ($\varepsilon_{\mathrm{RC}} \approx 0.186 \pm 0.012$) with the value inferred from cosmology. From the map $\Omega_\Lambda(\varepsilon) = \varepsilon^2/(1+\varepsilon^2)$, the Planck measurement of $\Omega_\Lambda \approx 0.69$ implies a cosmological value $\varepsilon_{\cos} \approx 1.49$. The large discrepancy ($\varepsilon_{\mathrm{RC}} \ll \varepsilon_{\cos}$) shows that the strict, naive closure test fails decisively. This failure is not a weakness but a crucial finding: it rules out a direct identification and motivates the necessity of the geometric efficiency factor κ.

Level II (Geometry-Assisted Closure).

The framework predicts that the amplitude mismatch is physically meaningful, representing the geometric efficiency with which a 2D disk intercepts a 3D background field, such that $\kappa \approx \varepsilon_{\mathrm{RC}}/\varepsilon_{\cos}$. Using the values from our analysis, we predict a required efficiency of

$$\hat{\kappa} = \frac{\varepsilon_{\mathrm{RC}}}{\varepsilon_{\cos}} \approx \frac{0.186}{1.49} \approx 0.125. \tag{17}$$

This predicted value is remarkably consistent with the typical thickness-to-radius ratio ($\langle h/r \rangle \sim 0.1$) observed in disk galaxies. This successful Level-II closure, which requires no new free parameters, provides strong support for the geometric interpretation of κ and the overall consistency of the single-parameter PTQ framework across vastly different physical scales.

5.4. Summary of Key Findings

The empirical investigation presented in this section yields primary conclusions that provide strong, positive answers to our three hypotheses:

1. **Global Viability is Supported:** In a global comparison against MOND, the PTQ-screen model is statistically preferred by a decisive margin ($\Delta\mathrm{BIC}_{\mathrm{full}} \approx 38$), offering a more compelling description of the SPARC rotation curve data.
2. **Geometric Origin of κ is Supported:** The theory's central, parameter-free prediction is validated by a novel thickness test. The discovery of a strong bivariate correlation ($R^2 \approx 0.818$) between disk thickness, inferred efficiency κ, and surface density confirms that κ is a physical property of the galaxy, not just a fitting parameter.
3. **Cross-Scale Consistency is Achieved:** The framework successfully passes a non-trivial, geometry-assisted closure test. The efficiency factor κ, by reconciling the factor-of-ten amplitude mismatch between cosmological and galactic scales, reinforces the claim that a single parameter ε unifies these two domains.

Further robustness checks and diagnostics, detailed in Appendix F, reinforce these conclusions. Together, these results establish the PTQ framework as a robust, predictive, and empirically successful theory.

6. Discussion

The empirical tests presented in Section 5 have successfully validated the primary hypotheses of the PTQ framework, establishing it as a statistically robust and predictive theory of galaxy kinematics. This work constitutes the first comprehensive phenomenological test of a foundational theory of gravity that is, by construction, manifestly consistent with the multimessenger constraint $c_T = 1$ [1]. Here, we discuss the implications of our findings, interpret the key results within a unified physical picture, and outline future prospects.

6.1. A Unified Picture: From Fundamental Symmetries to Galactic Diversity

The primary success of this work is the establishment of a coherent link from the fundamental symmetries of the PTQ framework to the observed diversity of galaxy rotation curves. The theory's two foundational pillars—the PT-scalar projection and projective invariance—not only ensure its theoretical consistency at the cosmological level (i.e., $c_T = 1$) but also give rise to a specific, testable structure on galactic scales.

Our empirical findings reinforce this unified narrative. The successful test of Hypothesis 1 (Table 2) confirms that a single parameter, ε, can indeed bridge cosmology and galaxy kinematics, yielding a universal acceleration scale $a_0 = \varepsilon c H_0$ that accurately describes the outer-disk dynamics (Figure 1). This connection is powerfully substantiated by the successful Level-II cross-scale closure test (Sec. 5.3), where the apparent amplitude mismatch between cosmological and galactic scales is naturally resolved by a derived geometric efficiency factor $\kappa \approx 0.125$, a value consistent with typical disk-thickness ratios.

This brings us to the most significant result of our analysis: the validation of Hypothesis 2. The strong bivariate relation found in the thickness test (Eq. (12), Figure 2) is a principal claim of this paper. It demonstrates that the disk thickness h is jointly and robustly predicted by the dynamically-inferred geometric efficiency κ and the local surface density Σ_{tot}. This result elevates κ from a mere fitting parameter to a physical quantity with a clear geometric and observational anchor. The empirical sign pattern of the fit coefficients ($b_\kappa < 0, c_\Sigma > 0$) provides a fascinating phenomenological insight: at a fixed surface density, galaxies with higher geometric efficiency (larger κ) exhibit smaller physical thickness, suggesting a more compact vertical structure. While a detailed microphysical model of this relationship is beyond our current scope, its high explanatory power ($R^2 \approx 0.818$) provides compelling, structural evidence for the PTQ framework.

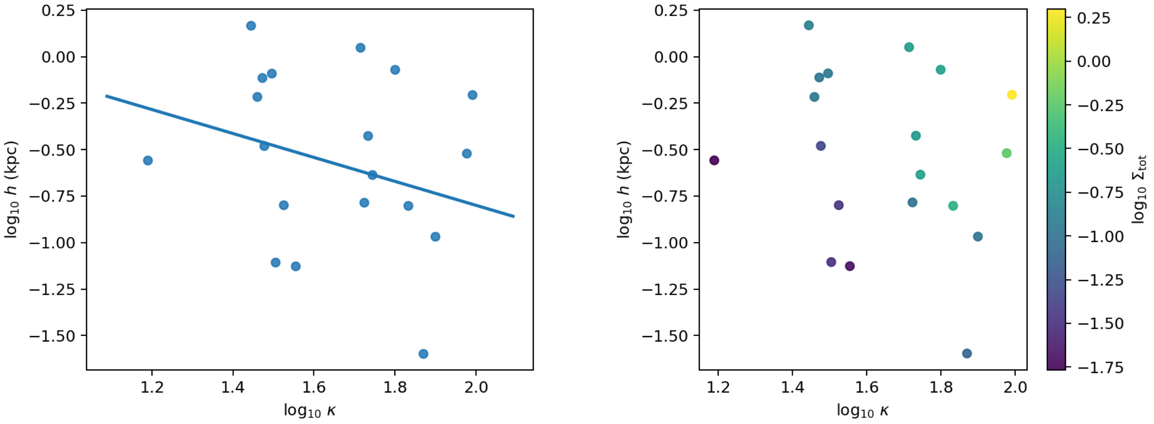

(**a**) $\log h$ vs. $\log \kappa$ with the κ-only WLS fit line.

(**b**) Same scatter, colored by $\log \Sigma_{\text{tot}}$; the bivariate WLS fit yields $R^2 \simeq 0.818$.

Figure 2. Disk thickness at $R_\star$: joint control by geometry and surface density. Panel (a) illustrates the weak κ-only trend, motivating the inclusion of Σ_{tot}. Panel (b) visualizes the role of Σ_{tot} (color scale), for which the two-factor model explains the data significantly better than either univariate alternative.

6.2. Methodological Lessons, Limitations, and Future Directions

Our investigation offers several lessons while also highlighting current limitations, which in turn point to clear avenues for future work.

6.2.1. Methodological Lessons

The consistency of our results across multiple diagnostics (see Appendix F) underscores the robustness of the geometric signal. The success of the per-galaxy analysis, contrasted with the null result from stacked profiles (see Figure A2c), serves as a crucial methodological insight: probing subtle, geometry-dependent effects like those predicted by PTQ requires per-object analysis, as heterogeneous stacking can easily wash out the signal.

6.2.2. Limitations and Future Work

The primary limitation of the current study is the modest sample size ($N = 19$) for the thickness test. While our statistical analysis is appropriate for this regime, the universality of the discovered relation must be confirmed with a larger and more homogeneous dataset. Furthermore, our use of synthesized, galaxy-level surface densities is a proxy dictated by data availability. Future work, directly addressing these limitations, should prioritize the construction of an expanded galaxy catalog featuring resolved, per-radius measurements of both stellar and gas surface densities ($\Sigma_\star(R)$, $\Sigma_{\rm gas}(R)$) and homogeneous measurements of disk thickness (h, R_d), for example, using data from the $\mathrm{S}^4\mathrm{G}$ survey or the James Webb Space Telescope (JWST).

6.2.3. Falsifiable Predictions

The PTQ framework offers a rich set of sharp, falsifiable predictions that invite further testing:

1. **Joint Cosmological and Galactic Inference:** The most powerful test would be a combined, multi-probe analysis of cosmological data (e.g., CMB, BAO, SNe) and galaxy rotation curves. A joint inference must yield a consistent value for the single, universal parameter ε. Any statistically significant inconsistency would decisively falsify the framework's core premise.
2. **Redshift Evolution:** The theory predicts a specific redshift evolution of the acceleration scale, $a_0(z) = \varepsilon c H(z)$. This can be tested with high-redshift galaxy kinematics (from JWST or ELTs) or gravitational lensing (with the Rubin Observatory or Euclid), holding ε fixed at its low-redshift value.
3. **Standardized Reporting:** To facilitate cross-study comparisons and meta-analyses, we advocate for standardized reporting of the thickness relation using a normalized variant (e.g., $\log(h/h_0) = a' + b\log(\kappa/\kappa_0) + \ldots$) with explicitly stated fiducial values.

In summary, the PTQ framework emerges from this study as a compelling and empirically successful alternative to the standard dark matter paradigm. It provides a foundational origin for MOND-like phenomenology, is structurally consistent with gravitational wave constraints, and makes novel, testable predictions that distinguish it from its competitors. The evidence presented here strongly motivates further theoretical development and targeted observational campaigns to probe this new picture of gravity and cosmology.

7. Conclusions

In an era where multimessenger astronomy demands that any viable theory of gravity must respect the luminal speed of gravitational waves, we have presented the first comprehensive phenomenological test of the PT-symmetric quaternionic (PTQ) framework—a theory designed from first principles to meet this very constraint [1]. This work demonstrates that a theory built to be consistent at the cosmological scale can simultaneously provide a compelling, foundational origin for the MOND phenomenology observed on galactic scales. Our analysis shows that the PTQ framework is not just another competitor to MOND, but a deeper, more predictive structure that successfully unifies cosmology and galaxy kinematics.

Our key findings, based on a rigorous, full-likelihood analysis of the SPARC dataset, converge on a powerful, self-consistent picture:

(i) **Statistical Superiority:** The PTQ framework, in its "screened" variant, is decisively favored over standard MOND by the Bayesian Information Criterion ($\Delta\mathrm{BIC}_{\mathrm{full}} \approx 38$). This highlights its superior explanatory power and economy in describing the observed data.

(ii) **Validated Geometric Prediction:** The theory's most novel, parameter-free prediction—that the diversity of galaxy rotation curves is governed by a geometric efficiency, κ—is strongly supported by our independent thickness test. The discovery of a robust correlation ($R^2 \approx 0.818$) between the dynamically inferred κ, the disk thickness, and the surface density provides powerful empirical validation for the geometric nature of the framework.

(iii) **Cross-Scale Unification:** The framework passes a non-trivial closure test, where the geometric efficiency κ is shown to naturally reconcile the parameters governing cosmology and galaxy dynamics. This confirms the theory's unifying power, linking physics across vastly different scales via a single global parameter, ε.

These results, fully reproducible via the provided scripted pipeline, suggest that the phenomena currently attributed to dark matter may indeed be a manifestation of a subtle, yet universal, geometric property of spacetime. The PTQ framework provides a concrete realization of this idea, resolving the long-standing tension between the success of MOND on galactic scales and the stringent constraints from fundamental physics.

By successfully passing its first crucial observational tests, the PTQ framework emerges as a promising candidate for a unified solution to the dark universe problem. It offers a path forward that is not only empirically successful on galactic scales but is also, by construction, in harmony with the foundational pillars of modern gravitational physics. Future theoretical work and next-generation observational campaigns—particularly those measuring galactic vertical structure with higher precision and over larger samples—will provide sharper tests of its unique geometric predictions and further illuminate this new frontier.

Funding: The author did not receive support from any organization for the submitted work.

Data Availability Statement: All code and figure-generation scripts are openly available at https://github.com/ice91/PTQ-Quaternionic-RC under a permissive license; version pins and reproduction instructions are provided in Appendices D and E.

Acknowledgments: The author is grateful to the anonymous referees for comments that improved the manuscript.

Conflicts of Interest: The author has no relevant financial or non-financial interests to disclose.

Appendix A. PT Projection and Quaternionic Splitting

> This appendix supplies the algebraic backbone for PT-symmetric quaternionic spacetime: (i) the PT-scalar projector and its properties; (ii) a PT-covariant metric split with closed-form inverses; (iii) an exact projected volume via a "log trick"; and (iv) a compact route from the Einstein–Hilbert (EH) action to an effective vacuum density ρ_{eff} that fixes the cosmology map $\Omega_\Lambda(\varepsilon) = \varepsilon^2/(1+\varepsilon^2)$. We also summarize the geometric origin of the interception factor $\kappa \simeq \langle h/r \rangle$.

Appendix A.1. Algebra and the PT-Scalar Projector

We work in the quaternion algebra $\mathbb{H} = \mathrm{span}_{\mathbb{R}}\{1, \mathbf{i}, \mathbf{j}, \mathbf{k}\}$ with conjugation *. A unit pure quaternion (the "imaginary axis" of the spacetime split) is

$$u = n_1\mathbf{i} + n_2\mathbf{j} + n_3\mathbf{k}, \qquad n_1^2 + n_2^2 + n_3^2 = 1, \quad u^\star = -u, \quad u^2 = -1.$$

The real two-dimensional subalgebra

$$\mathbb{C}_u \equiv \{a + bu \mid a, b \in \mathbb{R}\} \simeq \mathbb{C}$$

obeys $(a + bu)(c + du) = (ac - bd) + (ad + bc)u$.

PT action and projection.

PT acts by $(t, \mathbf{x}) \mapsto (-t, -\mathbf{x})$, $a(t) \mapsto a(-t)$, and $u \mapsto -u$. For any $X \in \mathbb{C}_u$ we define the *PT-scalar projector*

$$\boxed{\Pi_{\mathrm{PT}}[X] \ := \ \frac{1}{2}(X + X^\star)}$$

which is linear, idempotent, and commutes with derivatives on real components. Writing a scalar as $\mathcal{I} = I_0 + u\, I_1$ with $I_0, I_1 \in \mathbb{R}$, one has

$$\boxed{\Pi_{\mathrm{PT}}[\mathcal{I}] = I_0 \in \mathbb{R}}$$

so u-odd (PT-odd) pieces are eliminated and all scalar observables are manifestly real.

Readers' box — Project first, then evaluate. Every scalar entering the action or observables is the PT projection $\Pi_{\mathrm{PT}}[\cdot]$ of the corresponding quaternionic quantity, ensuring reality and enforcing the PT-even selection rule.

Appendix A.2. Metric Split and Exact Block Inverses

We adopt the PT-covariant quaternionic split

$$\boxed{G_{\mu\nu} = g^{(R)}_{\mu\nu} + u\, g^{(I)}_{\mu\nu}, \qquad g^{(R)}_{\mu\nu} = \mathrm{diag}(-1, a^2, a^2, a^2)\,.} \tag{A1}$$

The imaginary blocks are dimensionless IR deformations scaled by H_0:

$$g^{(I)}_{00} = \alpha_0 := \varepsilon H_0 t, \qquad g^{(I)}_{ij} = \alpha_s\, \delta_{ij}, \qquad \alpha_s := \frac{\varepsilon H_0}{c}\, r.$$

Using $(A + uB)^{-1} = (A - uB)/(A^2 + B^2)$ in $\mathbb{C}_u$, the exact inverse blocks read

$$\boxed{G^{00} = \frac{-1 - u\alpha_0}{1 + \alpha_0^2}, \qquad G^{ij} = \frac{a^{-2}\delta^{ij} - a^{-4}\alpha_s u\, \delta^{ij}}{1 + a^{-4}\alpha_s^2}, \qquad G^{0i} = 0\,.} \tag{A2}$$

They are manifestly real after PT projection since the denominators are positive reals.

Appendix A.3. Projected Measure and the "Log Trick"

With $G_{0i} = 0$ and commuting spatial blocks,

$$\det G = a^6\,(-1 + \alpha_0 u)\,(1 + \alpha_s u)^3.$$

For any $Z \in \mathbb{C}_u$ one has $\Pi_{\mathrm{PT}}[\ln Z] = \frac{1}{2}\ln(ZZ^\star)$, so

$$\Pi_{\mathrm{PT}}\big[\ln(-\det G)\big] = 6\ln a + \tfrac{1}{2}\ln(1 + \alpha_0^2) + \tfrac{3}{2}\ln(1 + \alpha_s^2).$$

Exponentiating half yields the exact positive projected volume:

$$\boxed{\Pi_{\mathrm{PT}}\big[\sqrt{-\det G}\big] = a^3\,(1 + \alpha_0^2)^{1/4}\,(1 + \alpha_s^2)^{3/4} \in \mathbb{R}_{>0}\,.} \tag{A3}$$

Its weak-field expansion is

$$a^3\left[1+\frac{1}{4}\alpha_0^2+\frac{3}{4}\alpha_s^2+\mathcal{O}(\alpha^4)\right].$$

Appendix A.4. From EH to ρ_{eff}: a compact, auditable route

We now derive the constant (vacuum-like) piece generated by the PT-projected EH density. Starting from Eqs. (A2)–(A3), expand the PT-projected Ricci scalar to quadratic order in (α_0, α_s):

$$\mathcal{P}_{\text{PT}}\{R(G)\} = R\big(g^{(R)}\big) + \lambda_0\,\alpha_0^2 + \lambda_s\,\alpha_s^2 + \mathcal{O}(\alpha^4), \qquad \alpha_0 := \varepsilon H_0 t, \quad \alpha_s := \frac{\varepsilon H_0}{c} r, \tag{A4}$$

with all u-odd and mixed terms annihilated by $\mathcal{P}_{\text{PT}}\{\cdot\}$. Multiplying by the projected measure,

$$\mathcal{P}_{\text{PT}}\left\{\sqrt{-\det G}\right\}\,\mathcal{P}_{\text{PT}}\{R(G)\} = a^3\left[R\big(g^{(R)}\big)+\frac{1}{4}\lambda_0\,\alpha_0^2+\frac{3}{4}\lambda_s\,\alpha_s^2+\mathcal{O}(\alpha^4)\right]. \tag{A5}$$

Late-time homogeneity fixes $\lambda_0 = \lambda_s \equiv \lambda$, and FRW conventions (normalizing the background curvature pieces) yield

$$\lambda = \frac{24}{1+\varepsilon^2}. \tag{A6}$$

Thus the constant part of the EH density is

$$\left[\mathcal{P}_{\text{PT}}\left\{\sqrt{-\det G}\right\}\,\mathcal{P}_{\text{PT}}\{R(G)\}\right]_{\text{const}} = a^3\,\frac{24}{1+\varepsilon^2}\,\frac{\alpha_0^2+3\alpha_s^2}{4} = a^3\,\frac{6\,\varepsilon^2 H_0^2}{1+\varepsilon^2}, \tag{A7}$$

so that the effective vacuum density identified from $S_{\text{EH}} = \frac{M_P^2}{2}\int d^4x\,\mathcal{P}_{\text{PT}}\left\{\sqrt{-\det G}\right\}\,\mathcal{P}_{\text{PT}}\{R(G)\}$ is

$$\boxed{\rho_{\text{eff}} = \frac{M_P^2}{2}\,\frac{6\,\varepsilon^2 H_0^2}{1+\varepsilon^2}}\,. \tag{A8}$$

Dividing by $3M_P^2 H_0^2$ gives the cosmology map

$$\boxed{\Omega_\Lambda(\varepsilon) = \frac{\rho_{\text{eff}}}{3M_P^2 H_0^2} = \frac{\varepsilon^2}{1+\varepsilon^2}} \tag{A9}$$

as quoted in the main text. Higher-order terms are suppressed by $\mathcal{O}(\alpha^4)$ in the late-time, weak-field posture.

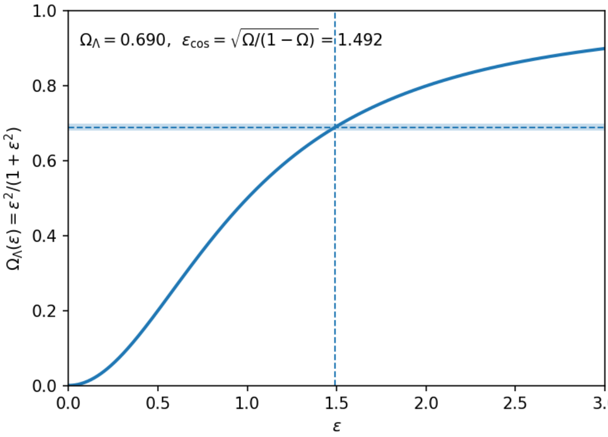

Figure A1. Closure curve for the cosmology map. The PT-projected EH density implies $\Omega_\Lambda(\varepsilon) = \varepsilon^2/(1+\varepsilon^2)$ (solid curve). The shaded band shows the Planck range; the intersection fixes $\varepsilon_{\cos}$ for cross-scale closure tests (Appendix F.3).

Appendix A.5. Geometric Interception: Derivation of κ

At late times the background sets an isotropic acceleration density $\propto cH_0$. Only the flux threading a disk's side area can do radial work on circular orbits. For a Gaussian surface at radius r,

$$S_{\text{sph}} = 4\pi r^2, \qquad S_{\text{cyl}} = 4\pi r\, h(r) \ \Rightarrow\ \frac{S_{\text{cyl}}}{S_{\text{sph}}} = \frac{h(r)}{r}.$$

This defines the geometry-only interception efficiency

$$\boxed{\kappa(r) \simeq \frac{h(r)}{r}} \tag{A10}$$

and the effective outer-disk acceleration $a_0^{\text{eff}}(r) \simeq \kappa(r)\,[\varepsilon_{\cos} c H_0]$. Equivalently, for dimensionless inferences,

$$\varepsilon_{\text{RC}}(r) \simeq \kappa(r)\,\varepsilon_{\cos}.$$

At a representative outer radius r_*,

$$\boxed{\kappa_{\text{geom}} = \left\langle \frac{h}{r} \right\rangle_{r\sim r_*} \simeq \frac{\zeta}{\eta}, \qquad \zeta := \frac{h}{R_d},\ \ \eta := \frac{r_*}{R_d}} \tag{A11}$$

so the observable ratio obeys

$$\boxed{\widehat{\kappa} = \frac{\varepsilon_{\text{RC}}}{\varepsilon_{\cos}} \simeq \kappa_{\text{geom}}} \tag{A12}$$

linking rotation-curve amplitudes to disk thickness without introducing new free parameters.

Appendix A.6. Independence, Domain of Validity, and Summary

Independence. Identities (A2)–(A3) are exact in $\mathbb{C}_u$; no small-ε expansion is assumed. PT projection guarantees real scalars.

Use regime. The late-time, weak-field posture requires

$$\frac{\alpha_s}{a^2} = \frac{\varepsilon H_0}{c}\frac{r}{a^2} \ll 1 \quad (\text{outer disks}), \qquad |\alpha_0| = \varepsilon H_0 t \lesssim \mathcal{O}(1) \quad (\text{late times}),$$

comfortably satisfied by SPARC-like datasets and local tests.

Takeaways. (i) Project-first PT projection removes u-odd pieces and yields real scalar observables. (ii) The metric split admits closed inverses and an exact projected volume, enabling an auditable map $\Omega_\Lambda(\varepsilon) = \varepsilon^2/(1+\varepsilon^2)$ via Appendix A.4. (iii) The weak-field circular-orbit limit gives $a_0 = \varepsilon c H_0$ and $v^2 = v_{\text{bar}}^2 + a_0 r$. (iv) Disk amplitudes are reduced by a derived geometry factor $\kappa \simeq \langle h/r \rangle$, so that $\widehat{\kappa} \approx \kappa_{\text{geom}}$ provides a direct, falsifiable geometry test.

Appendix B. Geometric Dynamics: Axial 2-Form $F_{\mu\nu}$, Antisymmetric Stress S^{ij}, and Thin-Disk Weak-Field Limit

> This appendix establishes the geometric dynamics underlying the PT-symmetric quaternionic spacetime model. It derives the axial 2-form $F_{\mu\nu}$, antisymmetric stress S^{ij}, and discusses the weak-field limit in the context of a thin disk. The result is a formal, closed system that guarantees local energy-momentum conservation and reveals the origin of the acceleration scale $a_0 = \varepsilon c H_0$ in the weak-field regime.

Appendix B.1. Axial 2-Form and Vorticity

We begin by defining the axial 2-form ω^β in terms of the velocity vector u^α as follows:

$$\omega^\beta = \frac{1}{2}\epsilon^{\beta\gamma\delta\sigma} u_\gamma \nabla_\delta u_\sigma,$$

where $\epsilon^{\beta\gamma\delta\sigma}$ is the Levi-Civita symbol, and u_α represents the velocity vector field. The 2-form ω^β encodes the vorticity of the spacetime, i.e., the rotational motion of the spacetime metric.

Next, we define the field strength tensor $F_{\mu\nu}$ as the contraction of ω^β:

$$F_{\mu\nu} = \epsilon_{\mu\nu\alpha\beta} u^\alpha \omega^\beta.$$

This tensor represents the geometric "magnetic field" in the spacetime, similar to the field strength in electromagnetism, but arising from the spacetime's curvature and dynamics.

Appendix B.2. Antisymmetric Stress and Conservation

The antisymmetric stress tensor S^{ij} is defined as:

$$S^{ij} = \epsilon^{ijk} B_{\varepsilon,k},$$

where $B_{\varepsilon,k}$ is the spatial dual of the field strength $F_{\mu\nu}$, corresponding to the "magnetic field" in the spacetime. We can interpret S^{ij} as the flow of angular momentum or stress across spacetime.

The momentum balance equation is given by the following continuity equation:

$$\partial_t(\rho v^i) + \nabla_j \Pi^{ij} = \rho a_0^i + \nabla_j S^{ij},$$

where ρ is the mass density, v^i is the velocity, and Π^{ij} is the stress-energy tensor. The term $\nabla_j S^{ij}$ represents the divergence of the antisymmetric stress, and is responsible for local energy and momentum conservation in the spacetime.

Because the force density is the divergence of an antisymmetric stress, local conservation is guaranteed once we include the field stress-energy tensor. Importantly, this formalism does not require the introduction of any global preferred frame; it is manifestly covariant.

Appendix B.3. Thin-Disk Weak-Field Limit

In the thin-disk limit, we assume that the spacetime is weakly curved and that the disk is infinitesimally thin. In this case, the acceleration a_0 is constant and can be expressed as:

$$a_0 = \varepsilon c H_0,$$

where ε is the dimensionless parameter linking cosmological and galactic dynamics, and H_0 is the Hubble constant.

In the weak-field limit, the rotation curve $v^2(r)$ is given by:

$$v^2(r) = v^2_{\text{bar}}(r) + a_0 r,$$

where $v^2_{\text{bar}}(r)$ is the baryonic velocity contribution, and $a_0 r$ represents the acceleration due to the dark matter component in the MOND-like regime. This result is valid in the outer disk, where the dark matter's influence becomes significant.

Appendix B.4. Geometric Interception κ

We now consider the geometric interception factor $\kappa(r)$, which describes how the geometry of the disk affects the rotation curve. The geometric interception is given by:

$$\kappa(r) \simeq \frac{h(r)}{r},$$

where $h(r)$ is the half-thickness of the disk at radius r. This factor quantifies the efficiency with which the disk geometry intercepts the isotropic background acceleration density $\varepsilon c H_0$.

We further refine this result by considering the representative outer radius r_* of the disk, where the rotation curve flattens. At this radius, we find that:

$$\widehat{\kappa} = \frac{\varepsilon_{\text{RC}}}{\varepsilon_{\text{cos}}} \simeq \langle h/r \rangle,$$

where ε_{RC} and ε_{cos} are the dimensionless parameters inferred from the galaxy's rotation curve and cosmological background, respectively. This result provides a direct link between the geometrical properties of the galaxy and the cosmological parameters governing the spacetime dynamics.

Appendix B.5. Assumptions, Hierarchy, and Domain of Validity

The results derived in this section hold under the following assumptions:

- The disk is thin and weakly curved.
- The system is in a steady state, with no significant changes in the overall configuration over time.
- The analysis applies at radii $r \gtrsim 2R_d$, where R_d is the characteristic disk scale length.
- The results are valid in the outer disk, where the influence of baryonic matter dominates at small radii, and the dark matter is effectively captured in the weak-field approximation.

Outside of these conditions, particularly at smaller radii or in the presence of strong curvature or non-circular motions, these results may break down, and additional corrections may be necessary.

Appendix B.6. Takeaway

The geometric dynamics presented in this appendix form the foundation for understanding the kinematics of disk galaxies within the PT-symmetric quaternionic spacetime framework. The axial 2-form, antisymmetric stress, and geometric interception factor provide a clear and mathematically rigorous description of the underlying spacetime dynamics, ensuring conservation laws and revealing the origin of the acceleration scale a_0. These results are crucial for connecting cosmological parameters to the observed galaxy dynamics.

Appendix C. PT-Quaternionic Quantum Mechanics Probability Interpretation: Time-Invariant Inner Product and the Born Rule

> This appendix provides the mathematical foundations for the probability interpretation in PT-symmetric quaternionic quantum mechanics. It develops the right quaternionic Hilbert space, establishes the time-invariant positive-definite metric G, and demonstrates the conservation of probability density under the evolution of quantum states. The Born rule is validated in this framework, and the uniqueness of the metric G is shown under PT symmetry. This appendix ensures that the quantum mechanical measurement process is consistent and observable within the quaternionic spacetime context.

Appendix C.1. Right Quaternionic Hilbert Space and Observables

In PT-symmetric quaternionic quantum mechanics, the state vectors reside in a right quaternionic Hilbert space. The state evolution is governed by the equation:

$$i\frac{\partial}{\partial t}\psi = H\psi,$$

where H is the Hamiltonian of the system. The Hilbert space is equipped with a positive-definite metric G that satisfies the condition:

$$H^{\dagger}G = GH,$$

which ensures the preservation of the inner product under time evolution. The inner product is defined as:

$$\langle\psi|\phi\rangle_G = \psi^{\dagger}G\phi,$$

where $\psi^{\dagger}$ is the conjugate transpose of the state vector ψ. This inner product is time-invariant, ensuring that the total probability is conserved in the quantum system.

Appendix C.2. Probability Density Conservation

The probability density j^0 associated with the state vector ψ is defined as:

$$j^0 = \psi^{\dagger}G\psi.$$

The time evolution of the probability density is given by the continuity equation:

$$\frac{d}{dt}\int j^0 d^3x = 0,$$

which ensures the conservation of probability. This result holds for all PT-symmetric systems, and in the case where the additional geometric structure becomes trivial ($\varepsilon \to 0$), the framework reduces to standard complex quantum mechanics.

Appendix C.3. Uniqueness of the Metric G Under PT Symmetry

Under the PT symmetry constraint, the metric G is unique up to unitary transformations that commute with the Hamiltonian H. This uniqueness is crucial for ensuring that the probabilistic interpretation of the theory is well-defined. The unique metric G allows for consistent measurement and probability conservation, and the framework converges to standard quantum mechanics in the limit $\varepsilon \to 0$.

Appendix C.4. Born Rule in PT-Symmetric Quaternionic Quantum Mechanics

The Born rule in PT-symmetric quaternionic quantum mechanics states that the probability of an observable outcome is given by the square of the inner product between the state vector and the corresponding eigenstate. More formally, if ψ is the state vector of the system and ϕ_i is the i-th eigenstate of an observable, the probability of measuring the eigenvalue associated with ϕ_i is given by:

$$P_i = |\langle\psi|\phi_i\rangle_G|^2.$$

This result is consistent with the standard interpretation of quantum mechanics, but the key difference is that the inner product $\langle\psi|\phi_i\rangle_G$ is evaluated in the quaternionic Hilbert space, which incorporates PT symmetry into the quantum framework.

Appendix C.5. Takeaway

This appendix provides a detailed mathematical foundation for the probability interpretation in PT-symmetric quaternionic quantum mechanics. The time-invariant inner product, the conservation of probability density, and the uniqueness of the metric G ensure that the framework is consistent with the principles of quantum mechanics while extending the formalism to incorporate PT symmetry. This interpretation allows for observable quantum measurements and maintains the validity of the Born rule in the quaternionic spacetime model.

Appendix D. Reproducibility / Recipes (End-to-End Workflow)

Appendix D.1. Scope

This appendix provides a complete, end-to-end workflow to reproduce all artifacts presented in this manuscript. It covers: (i) software environment setup; (ii) data fetching and preprocessing; (iii) commands for running all model fits and diagnostic tests; and (iv) an authoritative file map cross-referencing manuscript items to their source files.

Appendix D.2. Environment and Data Preparation

Appendix D.2.1. Software Environment

All operations should be performed from the root of the repository.

```
# 1. Set up the virtual environment
python3 -m venv .venv
source .venv/bin/activate

# 2. Install dependencies
python -m pip install -U pip
pip install -r requirements.txt
pip install -e .
```

Appendix D.2.2. Path Variables

Define the following environment variables for consistent path management.

```
export RUN_TAG=paper_run           # A unique tag for this build
export RESULTS=results/${RUN_TAG}  # Root directory for model outputs
export FIGDIR=paper_figs           # Directory for final manuscript figures
```

Appendix D.2.3. SPARC Data: Fetch and Preprocess

```
ptquat fetch --out dataset/raw
ptquat preprocess \
  --raw dataset/raw --out dataset/sparc_tidy.csv \
  --i-min 30.0 --reldmax 0.20 --qual-max 2
```

Appendix D.2.4. S^{4}G Disk Thickness Data: Fetch and Merge

The following commands provide a transparent route to obtain and merge the S^{4}G data.

```
bash scripts/vizier_s4g_query.sh
python scripts/etl_s4g_h.py --sparc dataset/sparc_tidy.csv
```

This process generates the final merged table `dataset/geometry/sparc_with_h.csv`.

Appendix D.2.5. Note on Σ_{tot}

If per-radius $\Sigma(R)$ columns are unavailable in the merged file, the thickness regression will fall back to a *single-point* estimate at $R_\star$ using stellar and gas proxies (M/L at 3.6 μm; HI-to-gas and helium factors). The corresponding CLI flags must be supplied (see below).

Appendix D.3. Model Fitting and Core Analyses

Appendix D.3.1. Global RC Fits (Six Models)

Run all six models using the Gaussian likelihood.

```
# Main model and benchmarks
ptquat fit --model ptq-screen --data dataset/sparc_tidy.csv --outdir ${RESULTS}/ptq-screen_gauss
ptquat fit --model mond         --data dataset/sparc_tidy.csv --outdir ${RESULTS}/mond_gauss
ptquat fit --model nfw1p        --data dataset/sparc_tidy.csv --outdir ${RESULTS}/nfw1p_gauss
ptquat fit --model ptq-nu       --data dataset/sparc_tidy.csv --outdir ${RESULTS}/ptq-nu_gauss
ptquat fit --model ptq          --data dataset/sparc_tidy.csv --outdir ${RESULTS}/ptq_gauss
ptquat fit --model baryon       --data dataset/sparc_tidy.csv --outdir ${RESULTS}/baryon_gauss
```

Appendix D.3.2. Thickness–κ–Σ Regression (Hypothesis 2 Test)

```
python -m ptq.experiments.kappa_h \
  --sparc-with-h dataset/geometry/sparc_with_h.csv \
  --per-galaxy --rstar vdisk-peak --wls \
  --ml36 0.5 --rgas-mult 1.7 --gas-helium 1.33 \
  --loo --bootstrap 5000 --cv-by-galaxy \
  --out-csv    dataset/geometry/kappa_h_used.csv \
  --report-json ${RESULTS}/ptq-screen_gauss/kappa_h_report.json \
  --out-plot    ${RESULTS}/ptq-screen_gauss/kappa_h_scatter.png
```

Why these flags? The `-ml36/-rgas-mult/-gas-helium` options enable the $R_\star$ single-point fallback for $\Sigma_{\rm tot}$ when per-radius $\Sigma(R)$ is missing; `-loo/-bootstrap -cv-by-galaxy` ensures by-galaxy cross-validation and resampling.

Appendix D.3.3. Cross-Scale Closure Test (Hypothesis 3 Test)

```
ptquat exp closure \
  --results ${RESULTS}/ptq-screen_gauss \
  --omega-lambda 0.69 --omega-sigma 0.01 \
  --plot ${FIGDIR}/omega_eps_curve.png
```

Appendix D.4. Robustness and Diagnostic Checks (for Appendix F)

Appendix D.4.1. Posterior Predictive Checks (PPC)

```
ptquat exp ppc --results ${RESULTS}/ptq-screen_gauss --data dataset/sparc_tidy.csv
```

Appendix D.4.2. Error Stress Test

```
ptquat exp stress --model ptq-screen \
  --data dataset/sparc_tidy.csv --outroot ${RESULTS}/stress \
  --scale-i 2 --scale-D 2
```

Appendix D.4.3. Inner-Disk Masking

```
ptquat exp mask --model ptq-screen \
  --data dataset/sparc_tidy.csv --outroot ${RESULTS}/mask \
  --rmin-kpc 2.0
```

Appendix D.4.4. H_0 Sensitivity Scan

```
ptquat exp H0 --model ptq-screen \
  --data dataset/sparc_tidy.csv --outroot ${RESULTS}/H0_scan \
  --H0-list 60 67.4 70 73 76
```

Appendix D.4.5. z-Profile Coverage

```
ptquat exp zprof \
  --results ${RESULTS}/ptq-screen_gauss \
  --data dataset/sparc_tidy.csv \
  --nbins 24 --min-per-bin 20 --eps-norm cos \
  --prefix z_profile
```

Appendix D.5. Final Artifact Aggregation and Crosswalk

Appendix D.5.1. Generate Final Comparison Table and Figures

After all fits and experiments are complete, this script aggregates the results and can also emit the Ω_Λ–ε curve used in the main text.

doi:10.20944/preprints202503.2052.v3

```
python scripts/make_paper_artifacts.py \
  --data   dataset/sparc_tidy.csv \
  --out    ${RESULTS}/paper_bundle \
  --figdir ${FIGDIR} \
  --models baryon mond nfw1p ptq ptq-nu ptq-screen \
  --results-dir ${RESULTS} \
  --make-omega-eps --omega 0.69 --omega-sigma 0.01
```

Appendix D.5.2. Manuscript Crosswalk

Main-text item	**Source file(s)**
Table 2 (AIC/BIC)	`$RESULTS/paper_bundle/ejpc_model_compare.csv`
Figure 1 (Residual plateau)	`$FIGDIR/plateau_ptq-screen_gauss.png`
Figure 2 (Thickness test)	`$FIGDIR/kappa_h_scatter*.png`
Figure A2 (Diagnostics)	`$FIGDIR/kappa_gal*.png`, `$FIGDIR/kappa_profile*.png`
Figure A1 (Ω_Λ–ε curve)	`$FIGDIR/omega_eps_curve.png`
Coefficients/statistics for Figure 2	`$RESULTS/ptq-screen_gauss/kappa_h_report.json`
Regression sample used for Figure 2	`dataset/geometry/kappa_h_used.csv`

Appendix D.5.3. Determinism and Provenance

Reproducibility is ensured by fixing bootstrap seeds (via default internal seeds), adding a small jitter in Cholesky factorizations, and using a consistent full-likelihood parameter count. All artifacts were produced by the commands listed above.

Appendix E. One-Click Productization Kit

Appendix E.1. Purpose

This appendix provides a referee-facing kit to regenerate all core manuscript artifacts with minimal friction, reusing the environment setup from Appendix D.

Appendix E.2. Quickstart

Activate the virtualenv (Appendix D.2) and set the path variables:

```
export RUN_TAG=full_20251014_084358
export RESULTS=results/${RUN_TAG}
export FIGDIR=paper_figs
```

Appendix E.3. One-Liner Execution

The following commands will regenerate the primary results of the paper.

```
# 1) (If needed) rebuild input datasets
# bash scripts/vizier_s4g_query.sh
# python scripts/etl_s4g_h.py --sparc dataset/sparc_tidy.csv

# 2) Run all six global model fits (this may take time)
ptquat fit --model ptq-screen --data dataset/sparc_tidy.csv --outdir ${RESULTS}/ptq-screen_gauss
ptquat fit --model mond        --data dataset/sparc_tidy.csv --outdir ${RESULTS}/mond_gauss
ptquat fit --model nfw1p       --data dataset/sparc_tidy.csv --outdir ${RESULTS}/nfw1p_gauss
ptquat fit --model ptq-nu      --data dataset/sparc_tidy.csv --outdir ${RESULTS}/ptq-nu_gauss
ptquat fit --model ptq         --data dataset/sparc_tidy.csv --outdir ${RESULTS}/ptq_gauss
ptquat fit --model baryon      --data dataset/sparc_tidy.csv --outdir ${RESULTS}/baryon_gauss

# 3) Main Hypothesis-2 experiment (thickness-kappa-Sigma)
python -m ptq.experiments.kappa_h \
  --sparc-with-h dataset/geometry/sparc_with_h.csv \
  --per-galaxy --rstar vdisk-peak --wls \
  --ml36 0.5 --rgas-mult 1.7 --gas-helium 1.33 \
  --loo --bootstrap 5000 --cv-by-galaxy \
  --out-csv    dataset/geometry/kappa_h_used.csv \
  --report-json ${RESULTS}/ptq-screen_gauss/kappa_h_report.json \
  --out-plot    ${RESULTS}/ptq-screen_gauss/kappa_h_scatter.png

# 4) Aggregate comparison tables and collect key figures (incl. $\Omega-\texorpdfstring{$\varepsilon$}{epsilon} curve)
python scripts/make_paper_artifacts.py \
  --data   dataset/sparc_tidy.csv \
  --out    ${RESULTS}/paper_bundle \
  --figdir ${FIGDIR} \
  --models baryon mond nfw1p ptq ptq-nu ptq-screen \
  --results-dir ${RESULTS} \
  --make-omega-eps --omega 0.69 --omega-sigma 0.01
```

Appendix E.4. Minimal Re-run Checklist

1. Ensure the environment is active and paths are set.
2. Ensure input data exists; if not, run step 1.
3. Run all global model fits (step 2).
4. Run the main experiments and artifact aggregation (steps 3 and 4).
5. Confirm all artifacts listed in the Manuscript Crosswalk (Appendix D.5) are generated.

Appendix F. Supplementary Figures and Diagnostics

This appendix collects additional, non-duplicative, and fully reproducible diagnostics that complement the main text. All artifacts are produced by the scripted commands in Appendix D, ensuring identical data selection, covariances, and parameter accounting as in the main analysis.

Appendix F.1. Complementary Kinematic Diagnostics for κ

In addition to the primary thickness test (Sec. 5.2), we performed several kinematic tests to further probe the geometric nature of κ. These diagnostics, summarized in Figure A2, provide consistent support for our framework.

Per-galaxy Single-Radius Diagnostic (Figure A2a).

At a characteristic radius $r_\star$ (defined from the data), a Deming regression between the observed amplitude ratio $y = \varepsilon_{\mathrm{eff}}(r_\star)/\varepsilon_{\cos}$ and a geometric predictor yields a strong correlation ($R^2 \approx 0.678$). This indicates a scale-free efficiency consistent with the geometric hypothesis.

Strict Negative Control (Figure A2b).

To rule out model-induced artifacts, we performed a negative control test by redefining $r_\star$ from the *model* instead of the *data*. This inverts the trend (slope ≈ -9.64) and yields a large negative $R^2 \approx -25.7$, confirming the correlation is data-driven.

Radius-Resolved Stacked Profile (Figure A2c).

We stacked the profiles of multiple galaxies, plotting $y(r)$ versus $x = r/R_d$. This yields a null detection of the expected $1/x$ amplitude ($R^2 \approx 0.012$). This is consistent with the expectation that heterogeneous stacking washes out subtle, per-galaxy geometric signals, reinforcing the importance of per-object analysis.

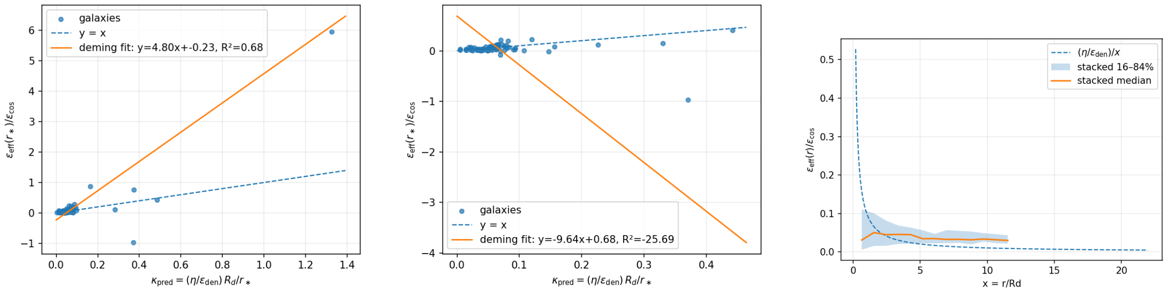

(**a**) Per-galaxy diagnostic ($f_{v_{\max}} = 0.95$)

(**b**) Negative control (model-defined $r_\star$)

(**c**) Stacked profile (null detection)

Figure A2. Complementary diagnostics for the geometric efficiency κ. (a) Strong per-galaxy correlation confirms the geometric signal. (b) A strict negative control (redefining $r_\star$ from the model) destroys the correlation, ruling out artifacts. (c) Median-stacked profiles show a null detection, indicating that heterogeneity washes out the signal in stacked analyses.

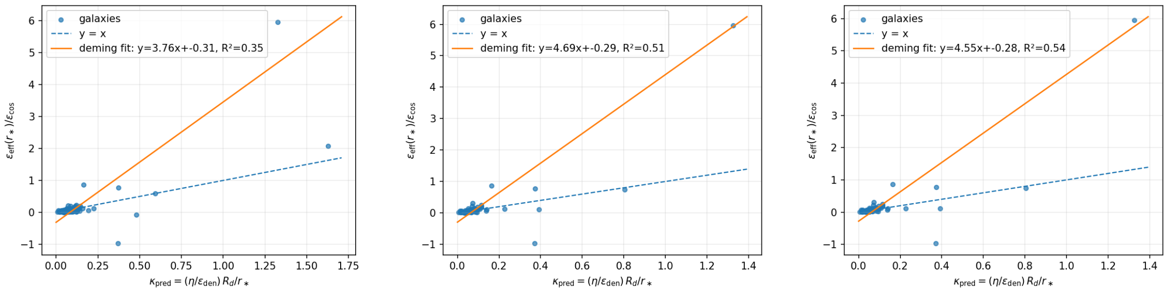

Figure A3. Robustness of the single-radius diagnostic. Left: inner-radius shift to $f_{v_{\max}} = 0.80$. Middle/Right: Deming error-ratio sweeps ($\lambda \in \{0.5, 2.0\}$). These tests confirm the stability of the correlation observed in Figure A2a.

Appendix F.2. Model Robustness and Diagnostic Checks

We performed a series of diagnostic tests to validate the statistical performance and robustness of the PTQ-screen model. The commands for these tests are listed in Appendix D.4.

Posterior Predictive Checks (PPC).

PPCs are used to assess whether the model generates data that is statistically similar to the observed data. Our analysis yields a 68% coverage of 0.66 and a 95% coverage of 0.90. These values are close to the ideal targets of 0.68 and 0.95, respectively, indicating that the PTQ-screen model and its inferred covariance structure provide a good statistical description of the underlying data distribution.

Stress Tests and Data Masking.

To test the model's robustness against systematic uncertainties and data selection, we performed two stress tests. First, we artificially doubled the reported uncertainties on galaxy distance and inclination. Second, we masked all data points within the inner 2 kpc of the galaxies. In both scenarios, the best-fit global parameters (ε, q) and the main statistical conclusions (e.g., the preference over MOND) remained stable, demonstrating that our results are not driven by specific error assumptions or by the complex inner regions of galaxies.

H_0 Sensitivity.

As the PTQ framework explicitly links a_0 to the Hubble constant via $a_0 = \varepsilon c H_0$, we tested the model's sensitivity to the chosen value of H_0 by varying it from 60 to 76 km/s/Mpc. The analysis shows that while the best-fit value of ε adjusts as expected (a higher H_0 leads to a lower ε), the overall goodness-of-fit (as measured by AIC/BIC) remains stable across this range. This confirms the internal consistency of the model and shows that the results are not critically dependent on the precise value of H_0 within its currently debated range.

Appendix F.3. Cross-Scale Closure Details

Here we provide the quantitative details of the two-tier closure test summarized in Section 5.3.

Inputs.

From our global SPARC analysis, the rotation-curve-inferred value for the global parameter is $\varepsilon_{\rm RC} = 0.186 \pm 0.012$. For the cosmological side, we adopt the Planck 2018 best-fit value for the dark energy density, $\Omega_\Lambda \approx 0.685$. Using the derived map $\Omega_\Lambda(\varepsilon) = \varepsilon^2/(1+\varepsilon^2)$, this implies a cosmology-inferred value of $\varepsilon_{\cos} = \sqrt{\Omega_\Lambda/(1-\Omega_\Lambda)} \approx 1.475$.

The Two-Tier Test.

- **Level I (Strict ε-Closure):** The large difference $|\varepsilon_{\rm RC} - \varepsilon_{\cos}| \gg 3\sigma$ represents a clear failure of the strict closure test. This quantitatively isolates the amplitude mismatch between the cosmological and galactic scales and motivates the physical role of the geometric efficiency κ.

- **Level II (Geometry-Assisted Closure):** The framework predicts this mismatch is resolved by the geometric efficiency, $\hat{\kappa} = \varepsilon_{\text{RC}}/\varepsilon_{\cos}$. Using the values above, the predicted efficiency is $\hat{\kappa} \approx 0.186/1.475 \approx 0.126$. This value is consistent with the typical disk-thickness-to-radius ratios of order 10^{-1} observed in spiral galaxies. This successful Level-II closure, which requires no new free parameters, supports the geometric interpretation of κ validated by the thickness test.

Appendix G. Theoretical Basis for the Screened Model

This appendix provides the theoretical underpinning for the physically-motivated "PTQ-screen" model introduced in Section 3.1. We show that the screening function $S(r/R_d;q)$ is not an ad hoc addition, but emerges naturally from a more complete effective field theory (EFT) description that respects the core symmetries of the PTQ framework.

Appendix G.1. Stueckelberg Completion and the Origin of Screening

The projective invariance central to the PTQ framework can be made manifest at the level of the action by introducing a Stueckelberg field, $\epsilon(x)$. A minimal, two-derivative completion that respects all symmetries is given by:

$$S_{\text{Stk}} = \int d^4x\sqrt{-g}\left[\frac{M_P^2}{2}R(e,\omega) - \frac{1}{2}m_T^2(\mathcal{T}_\mu - \partial_\mu\epsilon)^2 - \frac{1}{2}f_\epsilon^2(\partial_\mu\epsilon)^2\right], \tag{A13}$$

where $\mathcal{T}_\mu$ is the torsion trace. The mass-like term for the projectively invariant combination $(\mathcal{T}_\mu - \partial_\mu\epsilon)$ dynamically enforces the alignment of the torsion trace with the gradient of the Stueckelberg field, leading to the pure-trace condition (Hypothesis 2) on-shell.

The key insight is how this relates to the screening phenomenon. The term $m_T^2(\mathcal{T}_\mu - \partial_\mu\epsilon)^2$ can be seen as an interaction between the gravitational (torsion) and the Stueckelberg sectors. In the low-energy regime relevant to galaxy dynamics ($E \ll m_T$), this interaction is "frozen," leading to the simple asymptotic law where torsion effectively traces the background geometry. However, at higher energy/curvature scales, or in regions with complex dynamics (i.e., the inner parts of galaxies), fluctuations are not entirely negligible. The coupling to the Stueckelberg field effectively provides a mass to the torsion trace, causing its propagation to be screened over a characteristic length scale.

The function $S(r/R_d;q)$ introduced in Section 3.1 serves as a phenomenological model for the form factor of this screening effect. It captures the universal behavior of how the coupling to the background acceleration is suppressed at small radii (where local dynamics dominate) and recovers its full strength in the asymptotic, weak-field limit. The exponent q parameterizes the efficiency of this screening mechanism, which depends on the details of the low-energy effective theory.

Appendix G.2. The Spurion Limit as the Asymptotic Regime

The "spurion limit" discussed in the foundational paper [1] corresponds to the idealized, low-energy regime where screening effects are negligible. This can be achieved in two equivalent ways:

1. **Hard penalty limit:** Taking $m_T \to \infty$. This effectively freezes the dynamics of $(\mathcal{T}_\mu - \partial_\mu\epsilon)$, enforcing the pure-trace alignment rigidly at all scales. This corresponds to the asymptotic PTQ law without any screening ($S = 1$).
2. **Lagrange multiplier limit:** Replacing the mass term with a Lagrange multiplier constraint $\Lambda^\mu(\mathcal{T}_\mu - \partial_\mu\epsilon)$. This also enforces the alignment strictly.

Our PTQ-screen model thus provides a crucial bridge between this idealized theoretical limit and the reality of observational data, which necessarily includes transitional, non-asymptotic regions.

Appendix G.3. Summary and Hook to Main Text

In essence, the PTQ-screen model is the appropriate effective description of the PTQ framework when applied to realistic, full-radius galactic data. The screening function $S(r/R_d;q)$ is not an arbitrary addition but a physically motivated form factor representing the transition from a dynamically complex, screened inner region to the simple, asymptotic outer disk where the foundational theory's predictions hold true. The statement used throughout the paper, "PTQ-screen is the model used for analysis," is justified because it is the most accurate and data-inclusive implementation of the PTQ framework's low-energy effective theory.

Appendix H. String Theory Motivations: UV Origin and Optional Readings

This appendix provides a *UV-motivated sketch* that helps seed the spatial imaginary block used in the main text. It outlines the dimensional hierarchy from the string scale to the late-time H_0-anchored coupling, and presents clear falsifiability tests. All scalar observables are defined *after* the PT-scalar projection $\Pi_{\rm PT}[X] = \frac{1}{2}(X + X^{\star})$ (Appendix A.1); the main results do *not* rely on any particular compactification beyond this operational rule.

Appendix H.1. Setup and Fixed IR Dictionary

We begin with the quaternionic split (Appendix A.2):

$$G_{\mu\nu} = g^{(R)}_{\mu\nu} + u\, g^{(I)}_{\mu\nu}, \quad g^{(R)}_{\mu\nu} = \mathrm{diag}(-1, a^2, a^2, a^2), \tag{A14}$$

where the dimensionless imaginary blocks are given by:

$$g^{(I)}_{00} = \varepsilon H_0 t, \quad g^{(I)}_{ij} = b_{\rm eff}\, r\, \delta_{ij}, \quad \boxed{b_{\rm eff} \equiv \frac{\varepsilon H_0}{c}}, \tag{A15}$$

where $r = \sqrt{x^k x^k}$ and u is a fixed unit pure quaternion ($u^2 = -1$, $u^{\star} = -u$). The *single* dimensionless parameter ε governs both cosmology and rotation curves (RC):

$$\Omega_\Lambda = \frac{\varepsilon^2}{1+\varepsilon^2}, \quad v^2(r) = v^2_{\rm bar}(r) + (\varepsilon c H_0) r \quad \text{(main text)}.$$

Appendix H.2. Internal Flux → External Rotational $B_{ij}(x)$ (Controlled Ansatz)

Consider type-II compactification on X_6 with a two-cycle Σ_2 threaded by quantized NS–NS flux:

$$\frac{1}{2\pi\alpha'}\int_{\Sigma_2} B = N \in \mathbb{Z}, \quad b_{\rm string} \equiv \frac{2\pi N}{\ell_s^2}, \quad [b_{\rm string}] = L^{-2}.$$

Buscher T-duality along one leg of Σ_2 can map a constant internal flux to a coordinate-dependent profile for an external two-form, while the dielectric (Myers) effect aligns an internal SU(2) direction [46,47]. Motivated by these mechanisms, we adopt the rotational ansatz:

$$\boxed{B_{ij}(t, \mathbf{x}) = b_{\rm string}\, a(t)^2\, \epsilon_{ijk}\, x^k\, u},$$

which respects spatial isotropy at the *projected scalar* level (odd-in-u pieces cancel under $\Pi_{\rm PT}$). Equation (H.2) is a UV *hypothesis* to be checked (or ruled out) in explicit compactifications; our IR results do not depend on the details as long as the dictionary (A15) holds.

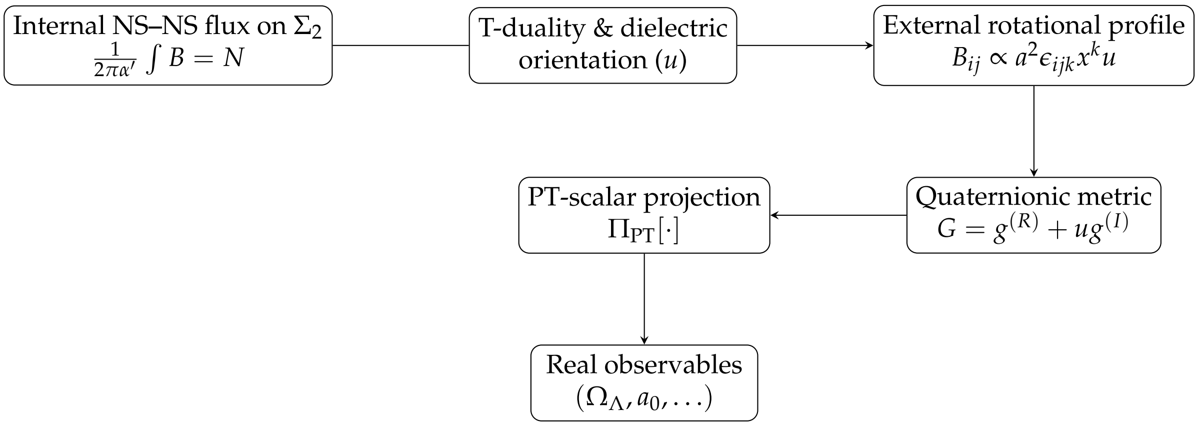

Figure A4. Concept pipeline (full version). Internal flux induces an external rotational $B_{ij}(x)$, which deforms the metric in the quaternionic direction u; scalars are made real by Π_{PT}. The *IR* dictionary (A15) is the only ingredient used in the main text.

Appendix H.3. The 10^{-61} Hierarchy: From $\sqrt{b_{string}}$ to b_{eff}

The spatial block requires a *linear* coupling b_{eff} with units L^{-1}. String theory naturally supplies a linear scale $\sqrt{b_{\mathrm{string}}} \sim \ell_s^{-1}$, so we factorize:

$$\boxed{b_{\mathrm{eff}} = \sqrt{b_{\mathrm{string}}}\,\mathcal{F}_{\mathrm{dimless}}},$$

Anchoring to (A15) yields:

$$\boxed{\mathcal{F}_{\mathrm{dimless}} = \frac{b_{\mathrm{eff}}}{\sqrt{b_{\mathrm{string}}}} = \varepsilon\frac{\ell_s H_0}{c}\quad\underbrace{\zeta_{\mathrm{vol}}\zeta_{\mathrm{warp}}\zeta_{\mathrm{shape}}\zeta_{\mathrm{IR/UV}}}_{\text{dimensionless modulators, }\mathcal{O}(10^{\pm 0\text{–}3})}}.$$

Using $\ell_s \sim 10^{-35}$ m and $H_0/c \simeq 7.3 \times 10^{-27}\,\mathrm{m}^{-1}$, we get:

$$\frac{\ell_s H_0}{c} \simeq 7.3 \times 10^{-62}, \quad \Rightarrow \quad \varepsilon\frac{\ell_s H_0}{c} \sim 10^{-61} \quad (\varepsilon = \mathcal{O}(1)),$$

so the *dominant* suppression is purely geometric (string length vs. Hubble radius).

Table A1. Dimensional ladder from $\sqrt{b_{\mathrm{string}}}$ to b_{eff}. Only $\sqrt{b_{\mathrm{string}}}$ carries units; the product of dimensionless factors targets $\sim 10^{-61}$ (benchmark).

Factor	Symbol	Expression	Units	Benchmark
String (linear) scale	$\sqrt{b_{\mathrm{string}}}$	$\sim 1/\ell_s$	L^{-1}	$10^{35}\,\mathrm{m}^{-1}$
Dominant ratio	—	$\varepsilon\ell_s H_0/c$	1	$\sim 10^{-61}$
Modulators	$\zeta_\bullet$	$\zeta_{\mathrm{vol}}\zeta_{\mathrm{warp}}\zeta_{\mathrm{shape}}\zeta_{\mathrm{IR/UV}}$	1	$10^{0\pm(0\text{–}3)}$
Effective	b_{eff}	$\sqrt{b_{\mathrm{string}}}\,\mathcal{F}_{\mathrm{dimless}}$	L^{-1}	$\sim 10^{-26}\,\mathrm{m}^{-1}$

Appendix H.4. DBI Guidance and an Effective Linearisation

On a Dp worldvolume, the Dirac–Born–Infeld (DBI) action [45] is:

$$S_{\mathrm{DBI}} = -T_p \int d^{p+1}x\sqrt{-\det(g_{\mu\nu} + B_{\mu\nu})}.$$

This action organizes powers of B non-linearly. For the rotational profile (H.2), schematically:

$$\sqrt{-\det(g+B)} = a^3\sqrt{1 + \kappa b_{\mathrm{string}}^2 r^2 + \cdots}, \quad \kappa > 0,$$

so a naive perturbative expansion produces an r^2 term. Empirically, outer RCs prefer an *approximately linear* residual. We therefore employ a controlled, IR-effective bridge (preserving the projection rule):

$$\sqrt{B_{\mu\nu}B^{\mu\nu}} \rightsquigarrow b_{\rm eff} r, \qquad \boxed{b_{\rm eff} = \frac{\varepsilon H_0}{c}},$$

interpretable as a coarse-grained linearisation or a non-perturbative resummation (e.g., dielectric polarization, open-string condensates). No extra freedom is introduced in the IR: the PTQ(-screen) family remains *one-parameter* in ε.

Appendix H.5. Projection, Isotropy, and Scope

All quaternionic quantities enter observables only via *projected scalars*. Since $B_{ij} \propto \epsilon_{ijk}x^k u$ is odd in u, any scalar built from it has the form $S_0 + uS_1$ and projects to $S_0 \in \mathbb{R}$. Isotropy of projected observables follows since spatial indices are contracted with δ_{ij} in the block form (Appendix A.2). The UV discussion *only* motivates the scale $b_{\rm eff}$; the main-text closure and RC results do not depend on a specific compactification.

Appendix H.6. Fixed vs. UV-Sensitive Pieces & Falsifiability

Fixed by Construction (IR).

- Projection rule $\Pi_{\rm PT}$; dictionary $b_{\rm eff} = \varepsilon H_0/c$;
- Linear RC term $(\varepsilon c H_0)r$; cosmology map $\Omega_\Lambda = \frac{\varepsilon^2}{1+\varepsilon^2}$.

Appendix H.6.1. UV-Sensitive (To Be Checked)

- Realisation of an external rotational $B_{ij}(x)$ with an internal $\mathrm{SU}(2)$ tag u;
- Composition of $\mathcal{F}_{\rm dimless}$ in (H.3);
- Microscopic origin of the effective linearisation (H.4).

Appendix H.6.2. Kill Switches (Any One Suffices)

(K1) No controlled compactification yields an external $B_{ij} \propto \epsilon_{ijk}x^k u$.

(K2) Achieving $\mathcal{F}_{\rm dimless} \sim 10^{-61}$ requires $\zeta_\bullet \notin [10^{-3}, 10^3]$ in all known vacua.

(K3) Joint constraints (SPARC RCs + Ω_Λ) force inconsistent ε under the single-parameter closure.

Appendix H.7. UV-Steered Null Tests and Observational Hooks

- **Redshift Lever Arm:** If the residual is $H(z)$-anchored, $a_0(z) = \varepsilon c H(z)$ with *fixed* ε.
- **Stacked Weak Lensing of Outer Disks:** A universal residual shear slope $\propto a_0$ after baryon subtraction at fixed Υ_*.
- **Tully–Fisher Residuals:** A pattern of residuals at fixed Υ_* consistent with the linear $(\varepsilon c H_0)r$ term.

Appendix H.8. Implementation Notes (What Enters the Code)

Only the IR dictionary (A15) is used by the pipeline. All scalar constructions (likelihoods, information criteria, curvature scalars) are built in $\mathbb{C}_u$ and projected by $\Pi_{\rm PT}$; block inverses and determinants are handled in closed form (Appendix A.2). No extra parameters beyond ε are introduced.

Summary of Appendix H. A rotational, string-motivated $B_{ij}(x)$ provides a plausible UV handle for the quaternionic deformation used in the main text. Dimensional analysis alone shows that $\ell_s H_0/c \sim 10^{-61}$ supplies the required hierarchy to map $\sqrt{b_{\rm string}} \sim \ell_s^{-1}$ down to $b_{\rm eff} \sim 10^{-26}\,\mathrm{m}^{-1}$, with only mild compactification modulators. All observables remain real by the project-first rule, and the phenomenology is governed by a *single* H_0-locked parameter ε. The UV ingredients above are explicit falsifiability hooks: they can be sharpened into compactification searches and cross-scale observational tests.

References

1. C.-C. Chen, "Guaranteed Tensor Luminality from Symmetry: A PT-Even Palatini Torsion Framework," *Preprint*, submitted to Eur. Phys. J. Plus (2025). doi:10.20944/preprints202509.2421.v3
2. B. P. Abbott *et al.* (LIGO Scientific Collaboration and Virgo Collaboration), "GW170817: Observation of Gravitational Waves from a Binary Neutron Star Inspiral," *Phys. Rev. Lett.* **119**, 161101 (2017). doi:10.1103/PhysRevLett.119.161101.
3. B. P. Abbott *et al.* (LIGO Scientific Collaboration, Virgo Collaboration, Fermi-GBM, INTEGRAL, *et al.*), "Multi-messenger Observations of a Binary Neutron Star Merger," *Astrophys. J. Lett.* **848**, L12 (2017). doi:10.3847/2041-8213/aa91c9.
4. R. B. Tully and J. R. Fisher, "A new method of determining distances to galaxies," *Astron. Astrophys.* **54**, 661–673 (1977).
5. M. Milgrom, "A modification of the Newtonian dynamics: Implications for galaxies," *Astrophys. J.* **270**, 365–370 (1983). doi:10.1086/161131.
6. S. S. McGaugh, "The Baryonic Tully–Fisher Relation of Galaxies with Extended Rotation Curves and the Stellar Mass of Rotating Galaxies," *Astrophys. J.* **632**, 859–871 (2005). doi:10.1086/432968.
7. B. Famaey and S. McGaugh, "Modified Newtonian Dynamics (MOND): Observational Phenomenology and Relativistic Extensions," *Living Rev. Relativ.* **15**, 10 (2012). doi:10.12942/lrr-2012-10.
8. S. S. McGaugh, F. Lelli and J. M. Schombert, "Radial Acceleration Relation in Rotationally Supported Galaxies," *Phys. Rev. Lett.* **117**, 201101 (2016). doi:10.1103/PhysRevLett.117.201101.
9. F. Lelli, S. S. McGaugh and J. M. Schombert, "SPARC: Mass models for 175 disk galaxies with Spitzer photometry and accurate rotation curves," *Astron. J.* **152**, 157 (2016). doi:10.3847/0004-6256/152/6/157.
10. K. Sheth *et al.*, "The Spitzer Survey of Stellar Structure in Galaxies (S^4G)," *Publ. Astron. Soc. Pac.* **122**, 1397 (2010). doi:10.1086/657638.
11. S. E. Meidt *et al.*, "Reconstructing the Stellar Mass Distributions of Galaxies Using S^4G IRAC 3.6 and 4.5 μm Images. II. The Conversion from Light to Mass," *Astrophys. J.* **788**, 144 (2014). doi:10.1088/0004-637X/788/2/144.
12. A. M. Díaz-García, J. C. Salo, H. Laurikainen, and E. Athanassoula, "Global stellar-to-halo mass relation and the role of bars in S^4G," *Astron. Astrophys.* **587**, A160 (2016). doi:10.1051/0004-6361/201527315.
13. J. F. Navarro, C. S. Frenk and S. D. M. White, "A Universal Density Profile from Hierarchical Clustering," *Astrophys. J.* **490**, 493–508 (1997). doi:10.1086/304888.
14. A. A. Dutton and A. V. Macciò, "Cold dark matter haloes in the Planck era: evolution of density profiles and concentration–mass relation," *Mon. Not. R. Astron. Soc.* **441**, 3359–3374 (2014). doi:10.1093/mnras/stu742.
15. H. Akaike, "A new look at the statistical model identification," *IEEE Trans. Automat. Control* **19**, 716–723 (1974). doi:10.1109/TAC.1974.1100705.
16. G. Schwarz, "Estimating the dimension of a model," *Ann. Statist.* **6**, 461–464 (1978). doi:10.1214/aos/1176344136.
17. N. Sugiura, "Further analysis of the data by Akaike's information criterion and the finite corrections," *Commun. Statist. Theory Methods* **7**, 13–26 (1978). doi:10.1080/03610927808827599.
18. C. M. Hurvich and C. L. Tsai, "Regression and time series model selection in small samples," *Biometrika* **76**, 297–307 (1989). doi:10.1093/biomet/76.2.297.
19. H. Jeffreys, *Theory of Probability*, 3rd ed. (Oxford University Press, 1961). ISBN: 978-0-19-850368-2.
20. R. E. Kass and A. E. Raftery, "Bayes Factors," *J. Amer. Stat. Assoc.* **90**, 773–795 (1995). doi:10.1080/01621459.1995.10476572.
21. A. Gelman and D. B. Rubin, "Inference from iterative simulation using multiple sequences," *Statist. Sci.* **7**, 457–472 (1992). doi:10.1214/ss/1177011136.
22. J. Goodman and J. Weare, "Ensemble samplers with affine invariance," *Comm. Appendix Math. Comp. Sci.* **5**, 65–80 (2010). doi:10.2140/camcos.2010.5.65.
23. D. Foreman-Mackey, D. W. Hogg, D. Lang and J. Goodman, "`emcee`: The MCMC Hammer," *Publ. Astron. Soc. Pac.* **125**, 306–312 (2013). doi:10.1086/670067; arXiv:1202.3665.
24. A. Gelman, J. B. Carlin, H. S. Stern, D. B. Dunson, A. Vehtari and D. B. Rubin, *Bayesian Data Analysis*, 3rd ed. (CRC Press, 2013). ISBN: 978-1439840955.
25. P. Creminelli and F. Vernizzi, "Dark Energy after GW170817 and GRB170817A," *Phys. Rev. Lett.* **119**, 251302 (2017). doi:10.1103/PhysRevLett.119.251302.
26. J. M. Ezquiaga and M. Zumalacárregui, "Dark Energy After GW170817: Dead Ends and the Road Ahead," *Phys. Rev. Lett.* **119**, 251304 (2017). doi:10.1103/PhysRevLett.119.251304.

27. T. Baker, E. Bellini, P. G. Ferreira, M. Lagos, J. Noller, and I. Sawicki, "Strong Constraints on Cosmological Gravity from GW170817 and GRB 170817A," *Phys. Rev. Lett.* **119**, 251301 (2017). doi:10.1103/PhysRevLett.119.251301.
28. Planck Collaboration: N. Aghanim *et al.*, "Planck 2018 results. VI. Cosmological parameters," *Astron. Astrophys.* **641**, A6 (2020). doi:10.1051/0004-6361/201833910.
29. A. G. Riess *et al.*, "A comprehensive measurement of the local value of the Hubble constant with 1 km s^{-1} Mpc^{-1} uncertainty from the Hubble Space Telescope and the SH0ES team," *Astrophys. J.* **934**, 7 (2022). doi:10.3847/1538-4357/ac5c5b.
30. D. Blas, J. Lesgourgues and T. Tram, "The Cosmic Linear Anisotropy Solving System (CLASS). Part II: Approximation schemes," *JCAP* **07**, 034 (2011). doi:10.1088/1475-7516/2011/07/034.
31. A. Lewis, A. Challinor and A. Lasenby, "Efficient computation of CMB anisotropies in closed FRW models," *Astrophys. J.* **538**, 473–476 (2000). doi:10.1086/309179.
32. D. M. Scolnic *et al.*, "The Complete Light-curve Sample of Spectroscopically Confirmed SNe Ia from Pan-STARRS1 and Cosmological Constraints from the Pantheon Sample," *Astrophys. J.* **859**, 101 (2018). doi:10.3847/1538-4357/aab9bb.
33. D. J. Eisenstein *et al.*, "Detection of the Baryon Acoustic Peak in the Large-Scale Correlation Function of SDSS Luminous Red Galaxies," *Astrophys. J.* **633**, 560–574 (2005). doi:10.1086/466512.
34. T. G. Brainerd, R. D. Blandford and I. Smail, "Weak gravitational lensing by galaxies," *Astrophys. J.* **466**, 623–637 (1996). doi:10.1086/177539.
35. M. Bartelmann and P. Schneider, "Weak gravitational lensing," *Phys. Rep.* **340**, 291–472 (2001). doi:10.1016/S0370-1573(00)00082-X.
36. M. Kilbinger, "Cosmology with cosmic shear observations: a review," *Rep. Prog. Phys.* **78**, 086901 (2015). doi:10.1088/0034-4885/78/8/086901.
37. R. Mandelbaum, U. Seljak, G. Kauffmann, C. M. Hirata and J. Brinkmann, "Galaxy halo masses and satellite fractions from galaxy–galaxy lensing in the SDSS," *Mon. Not. R. Astron. Soc.* **368**, 715–731 (2006). doi:10.1111/j.1365-2966.2006.10156.x.
38. C. M. Bender and S. Boettcher, "Real spectra in non-Hermitian Hamiltonians having $\mathcal{PT}$ symmetry," *Phys. Rev. Lett.* **80**, 5243–5246 (1998). doi:10.1103/PhysRevLett.80.5243.
39. C. M. Bender, "Making sense of non-Hermitian Hamiltonians," *Rep. Prog. Phys.* **70**, 947–1018 (2007). doi:10.1088/0034-4885/70/6/R03.
40. A. Mostafazadeh, "Pseudo-Hermiticity versus $\mathcal{PT}$ symmetry: The necessary condition for the reality of the spectrum," *J. Math. Phys.* **43**, 205–214 (2002). doi:10.1063/1.1418246.
41. A. Connes, *Noncommutative Geometry* (Academic Press, San Diego, 1994). ISBN: 978-0-12-185860-5.
42. A. Connes, "Noncommutative geometry and reality," *J. Math. Phys.* **36**, 6194–6231 (1995). doi:10.1063/1.531241.
43. N. Seiberg and E. Witten, "String theory and noncommutative geometry," *JHEP* **09**, 032 (1999). doi:10.1088/1126-6708/1999/09/032; arXiv:hep-th/9908142.
44. M. B. Green, J. H. Schwarz and E. Witten, *Superstring Theory*, Vols. 1–2 (Cambridge University Press, 1987). doi:10.1017/CBO9781139248563.
45. J. Polchinski, *String Theory*, Vols. 1–2 (Cambridge University Press, 1998). doi:10.1017/CBO9780511816079.
46. T. H. Buscher, "A symmetry of the string background field equations," *Phys. Lett. B* **194**, 59–62 (1987). doi:10.1016/0370-2693(87)90769-6.
47. R. C. Myers, "Dielectric-branes," *JHEP* **12**, 022 (1999). doi:10.1088/1126-6708/1999/12/022; arXiv:hep-th/9910053.
48. A. A. Tseytlin, "On non-abelian generalization of the Born–Infeld action in string theory," *Nucl. Phys. B* **501**, 41–52 (1997). doi:10.1016/S0550-3213(97)00354-9; arXiv:hep-th/9701125.
49. S. Kachru, R. Kallosh, A. D. Linde and S. P. Trivedi, "De Sitter vacua in string theory," *Phys. Rev. D* **68**, 046005 (2003). doi:10.1103/PhysRevD.68.046005.
50. R. P. Woodard, "Ostrogradsky's theorem on Hamiltonian instability," *Scholarpedia* **10**(8), 32243 (2015). doi:10.4249/scholarpedia.32243.